Institute for Systems Theory and Automatic Control
Institut für Systemtheorie und Regelungstechnik
Universität Stuttgart
Prof. Dr.-Ing. Frank Allgöwer
Pfaffenwaldring 9
70550 Stuttgart
Germany

IST-Internal Report

PIECEWISE-LINEAR MAP FOR STUDYING BORDER-COLLISION PHENOMENA IN DC/AC CONVERTERS

Authors: V. Avrutin, Zh.T. Zhusbalyiev

Scope: Project "Generic bifurcation structures in piecewise-smooth maps with extremely high number of borders in theory and applications for power converter systems", funded by DFG, AV 111/2-1

Date: 2019-04-20

Status: submitted for publication in Int. J. Bifurcat. & Chaos

PIECEWISE-LINEAR MAP FOR STUDYING BORDER-COLLISION PHENOMENA IN DC/AC CONVERTERS

VIKTOR AVRUTIN

Institute for Systems Theory and Automatic Control, University of Stuttgart, Pfaffenwaldring 9, 70550 Stuttgart, Germany

avrutin@ist.uni-stuttgart.de

ZHANYBAI T. ZHUSUBALIYEV

Department of Computer Science, Southwest State University, 50 Years of October Str. 94, 305040, Kursk, Russia

zhanybai@hotmail.com

Recently, while studying the dynamics of power electronic DC/AC converters we have demonstrated that the behavior of these systems can be modeled by piecewise-smooth maps which belong to a specific class of models not investigated before. The characteristic feature of these maps is the presence of a very high number of switching manifolds (border points in 1D). Obviously, the multitude of control strategies applied in the modern power electronics leads to different maps belonging to this class of models. However, in this paper we show that several of the models can be studied using the same piecewise-linear approximation, so that the bifurcation phenomena which can be observed in this model are generic for many models. Based on the results obtained before for piecewise-smooth models with different kinds of nonlinearities resulting from the corresponding control strategies, in the present paper we discuss the generic bifurcation patterns in the underlying piecewise-linear map.

Keywords: piecewise-smooth systems; piecewise-linear map, border collisions; power electronic DC/AC converters; degenerate fold and pitchfork bifurcations

1. Introduction

Many problems in engineering and applied science lead us to consider piecewise-smooth maps. Examples of such systems include relay and pulse-width modulated control systems, power electronics systems [Banerjee & Verghese, 2001; Zhusubaliyev & Mosekilde, 2003; di Bernardo *et al.*, 2008b], mechanical systems with dry friction or impacts [Armstrong-Hélouvry *et al.*, 1994; Brogliato, 1999; Leine & Nijmeijer, 2013], as well as any kind of systems involving thresholds, constrains and decision making processes in economics and social sciences [Puu & Sushko, 2006; Mosekilde & Laugesen, 2007; Bischi *et al.*, 2010].

In such systems, as a parameter is varied, an invariant set such as, for example, a fixed point or a cycle, may collide with a switching set where the equations governing the dynamics change. When such a collision causes a qualitative change in the dynamics, a special dynamic phenomenon occurs, referred to as a border-collision bifurcation. An overview of border collision related phenomena can be found in [di Bernardo *et al.*, 2008a,b].

Recently, we have studied a variety of problems associated with border-collision phenomena in power electronic DC/AC converters (inverters) [Avrutin *et al.*, 2015, 2016, 2017b,a]. Converters of this type are applied to provide AC voltage or current of a specified amplitude and frequency from a DC source. By virtue of their high efficiency and relatively low costs, inverters have achieved widespread application in modern power engineering. Standard examples of devices that include inverters are uninterruptible power supplies (UPS), active filters, flexible AC transmission systems (FACTS), voltage compensators, and so on [Rashid & Luo, 2006]. Moreover, in the last few years the interest in inverters has been continuously increasing because of their use in applications related to renewable energy sources, such as solar panel systems and wind turbines [Singh, 2013; Hassaine *et al.*, 2014; Jain *et al.*, 2015; Alexander, 2016; Sayigh, 2016], as well as in the power supply systems of electric and hybrid cars [Poullikkas, 2015].

The dynamics of an inverter system is governed by two external signals: a low frequency reference signal that defines the waveform of the desired output voltage or current, and a high frequency, pulse-modulated switching signal. The ratio m between these frequencies is referred to as the *frequency modulation ratio*. Typically, it takes the values of the magnitude between 10^2 and 10^3. It has been shown in our recent publications that the presence of two vastly different frequencies causes several unusual phenomena to occur, such as transitions to chaos via irregular cascades of border collisions [Avrutin *et al.*, 2015], structures in parameter space formed by persistence border collisions inside the domain of regular dynamics [Avrutin *et al.*, 2016], and a global alignment of the boundaries associated with smooth bifurcations [Avrutin *et al.*, 2017b].

The mechanisms leading to these phenomena are related to specific properties of the underlying models. Indeed, in the cited works we presented a generic two-step approach for modeling of inverter systems. The first step of this approach involves the calculation of a *primary stroboscopic mapping* with the sampling step determined by the high switching frequency. Because of the presence of the low frequency signal, the primary stroboscopic map is non-autonomous. Thereafter, the second step of the modeling approach consists in the calculation of a *secondary stroboscopic mapping* with the sampling step determined by the low frequency. Provided that the frequency modulation ratio is an integer number, the secondary stroboscopic map is given by the iterate of the primary stroboscopic map which corresponds to one period of the low frequency signal (i.e., the m-th iterate). By construction (as the sampling step is chosen to be identical with the period of the low frequency signal), the secondary stroboscopic map is autonomous.

Due to a high value of m, the resulting model (the secondary stroboscopic map) belongs to a specific class of piecewise-smooth maps barely investigated before. The characteristic feature of maps belonging to this class is an extremely high number of the switching manifolds separating the branches of the function which governs the dynamics. This follows immediately from the fact that for any piecewise-smooth map the number of branches of the m-th iterate grows exponentially with m. At present, the dynamics of such maps is not yet fully covered by the existing theory.

Remarkably, the models of the inverters considered in the cited works show certain similarities. Indeed, the primary stroboscopic maps of these systems are defined by two linear branches related to the saturation of the duty cycle of the circuit, and a nonlinear branch corresponding to the normal operational regime. The specific kind of nonlinearity of this branch is determined by the applied control strategy. However, due to the high value of m, the influence of this nonlinearity on the branches of the secondary stroboscopic mapping turns out to be relatively weak. Therefore, it is quite natural to consider a piecewise-linear approximation of the primary stroboscopic map. By construction, this approximation is common for a broad class of inverter systems which have similar structural principles and differ in the applied control strategies only. As shown below, this approximation can be seen as a generic template for many inverter systems such as, for instance, H-bridge inverters with different types of bipolar and unipolar sinusoidal pulse-width modulated (PWM) control. Accordingly, it appears to be promising first to study the bifurcation phenomena in the piecewise-linear model, and then to consider the corresponding phenomena in the applied systems modeled by maps with nonlinear branches as a kind of deformation of these – more generic – structures. The advantages of this mode of operation are clearly in the commonality of the piecewise-linear map and the possibility to obtain for this map more analytic results than for maps with nonlinear branches. Still, the question arises how well the piecewise-linear model approximates the dynamics of maps with nonlinear branches.

As a consequence, the goals of this paper are twofold. On one hand, we aim to determine which bifurcation phenomena already observed in other piecewise-smooth models composed by nonlinear functions exist in the piecewise-linear approximation. Such phenomena can be seen as generic in the sense that similar effects will be present in all models which can be sufficiently well approximated by the piecewise-linear model. On the other hand, we are interested in the question which phenomena are specific for the piecewise-linear map and up to which extent the linearity of the function provides the possibility for analytic results which cannot be obtained in a closed form for nonlinear functions.

The paper is organized as follows. First, in Sec. 2, we describe three different inverter systems which can be modeled by piecewise-smooth maps with a nonlinear branch. Eventually, we introduce a single piecewise-linear map which represents an approximation for all three models considered before. Thereafter, in Sec. 3, we discuss the bifurcation structures observed in a 2D parameter plane of this piecewise-linear map, focusing on two types of events most characteristic for such maps, namely border collisions, which occur when a fixed point or cycle collides with a boundary between partitions in the state space (Sec. 3.2), and degenerate bifurcations, occurring when a fixed point or cycle changes its stability (Sec. 3.3). Finally, in Sec. 4 we compare the results obtained for the piecewise-linear approximation with the results already knows for underlying maps with nonlinear branches, identifying bifurcations patters generic for the considered class of inverter systems.

2. Description of the system

Among a large variety of industrially applied inverter systems, we consider two common types of these systems, namely single-phase H-bridge and multi-level inverters. These two types of systems cover a broad spectrum of applications ranging from low power devices for chargers in household equipment to megawatt applications used in the main power supply lines. In the meantime, several modulation techniques have been developed for control of inverter systems. Wide-spread among them are the bipolar and unipolar sinusoidal pulse width modulation (SPWM) techniques.

Below we consider three typical models of inverters belonging to these types (a bipolar and an unipolar single-level H-bridge inverters as well as a multi-level unipolar H-bridge inverter) and demonstrate that – despite the differences in the underlying circuits – the similarities in their behavior can be explained by the same piecewise-linear approximation these models lead to.

2.1. *Bipolar H-bridge inverter*

The first model considered below describes the behavior of the bipolar H-bridge inverter [Espinoza, 2011] shown schematically in Fig. 1(a). The four switches S_j, $j = 1, \ldots, 4$, of the bridge structure operate in pairs so that S_1 and S_4 are closed when S_2 and S_3 are open, and *vice versa*. In the first case, a positive voltage E_0 is applied to the load, while in the second case this voltage is reversed. The switches are controlled by the sinusoidal PWM modulator through a feedback mechanism as illustrated in Fig. 1(b).

In order to generate the switching signals to the pairs of switches S_1, S_4 and S_2, S_3, the corrector amplifier DA_2 determines the error signal $\xi(t) = \alpha(V_{\mathrm{ref}}(t) - V_{\mathrm{cs}}(t))$ where $V_{\mathrm{ref}}(t) = V_m \cdot \cos(2\pi t/T)$ is the reference sinusoidal voltage, and $V_{\mathrm{cs}}(t) = \beta i(t)$ is the output voltage of the current sensor CS, and $i(t)$ is the current of the RL (resistive-inductive) load. Here, α is referred to as the corrector gain factor and β is the current sensor sensitivity; while V_m and $T = ma$ are the amplitude and the period of the reference signal, respectively. The value a is one ramp period (the period of the clock signal V_{clock}) and m is the frequency modulation ratio, i.e., the number of clock cycles during the period T of the reference signal. In the following we assume m to be an integer number. As shown in our previous publications [Avrutin *et al.*, 2015, 2017b], the dynamics of the inverter depends on whether m is even or odd.

According to the pulse width modulation approach of the first kind (PWM-1), the sample-and-hold unit S/H reads the error signal $\xi(t)$ at every clock time $t = ka$, $k = 0, 1, 2 \ldots$, and maintains it for the following switching period $[ka, (k+1)a)$ (see Fig. 1(b)). This determines the control signal $V_{\mathrm{con}}(t)$. In order to generate the switching signals to the pairs of switches S_1, S_4, and S_2, S_3, the comparator DA_1 compares the signal $V_{\mathrm{con}}(t)$ with a periodic ramp function $V_{\mathrm{ramp}}(t)$. If long as $V_{\mathrm{con}}(t) > V_{\mathrm{ramp}}(t)$, switches S_1, S_4 are open and S_2, S_3 are closed. Otherwise the switches S_1, S_4 are closed and S_2, S_3 open.

The ramp function $V_{\mathrm{ramp}}(t)$ varies in synchrony with the clock signal in the range between $-V_0$ and $+V_0$. If $V_{\rm con}(t) \geqslant +V_0$ or $V_{\rm con}(t) \leqslant -V_0$, the modulator is saturated. In the first case, the duration of the positive pulse is equal to the ramp period a, and in the second case it is equal to zero, as shown in Fig. 1(b).

The dynamics of the inverter system described above can be represented by the following non-autonomous differential equation with a discontinuous right hand side:

$$L\frac{di}{dt} = \begin{cases} -R\,i + E_0 & \text{if} \quad V_{\rm con}(t) > V_{\rm ramp}(t), \\ -R\,i - E_0 & \text{if} \quad V_{\rm con}(t) < V_{\rm ramp}(t). \end{cases} \tag{1a}$$

Here,

$$V_{\rm ramp}(t) = 2V_0\left(t/a - \lfloor t/a \rfloor - \tfrac{1}{2}\right), \tag{1b}$$
$$V_{\rm con}(t) = \xi(t)|_{t=a\lfloor t/a \rfloor}, \tag{1c}$$
$$\xi(t) = \alpha(V_{\rm ref}(t) - \beta i(t)), \tag{1d}$$
$$V_{\rm ref}(t) = V_m \cos\left(\frac{2\pi t}{ma}\right). \tag{1e}$$

The number $\lfloor t/a \rfloor$ denotes the largest integer not greater than t/a (i.e., the integer part, or floor, of t/a).
Next, let us introduce the dimensionless state variable $x = \dfrac{Ri}{E_0}$, the dimensionless time variable $\bar{t} = \dfrac{t}{a}$ and the set of dimensionless parameters:

$$P = \frac{R}{\beta E_*}V_0,\ q = \frac{R}{\beta E_*}V_m,\ \lambda = -\frac{R}{L}a,\ \Gamma = \frac{E_0}{E_*}.$$

The parameter P controls the amplitude of the ramp function, q is the amplitude of the reference voltage, and Γ represents the voltage of the DC source, all normalized with respect to $E_* = 1\ V$. The absolute value of λ is proportional to the reciprocal of the time constant of the converter filter, normalized with respect to the period a of the ramp signal.
In these terms, Eq. (1) can be rewritten as

$$\dot{x} = \begin{cases} \lambda(x-1) & \text{if } \varphi(\bar{t}, x) > 0, \\ \lambda(x+1) & \text{if } \varphi(\bar{t}, x) < 0, \end{cases} \tag{2a}$$

where $\dot{x}$ denotes the derivative of x with respect to $\bar{t}$. The scalar function

$$\varphi(\bar{t}, x) = \frac{q}{\Gamma}\cos\left(\frac{2\pi\lfloor\bar{t}\rfloor}{m}\right) - x(\bar{t})\Big|_{\bar{t}=\lfloor\bar{t}\rfloor} - \eta(\bar{t}) \tag{2b}$$

with

$$\eta(\bar{t}) = \frac{2P}{\alpha\Gamma}\left(\bar{t} - \lfloor\bar{t}\rfloor - \tfrac{1}{2}\right), \tag{2c}$$

defines the switching manifold

$$\Sigma = \left\{(\bar{t}, x) \mid \varphi(\bar{t}, x) = 0\right\}. \tag{2d}$$

This manifold separates the phase space of Eq. (2) in two partitions in which the dynamic behavior of the system is governed by different vector fields. As shown in [Avrutin *et al.*, 2015], all solutions to Eq. (2) intersect the switching manifold Σ transversely.
The function $\varphi(\bar{t})$ represents the normalized control signal $V_{\rm con}(t)$, i.e., the output signal of the sample-and-hold unit S/H. The saw-tooth function $\eta(\bar{t})$ is a periodically repeated ramp function with the ramp period 1, i.e., $\eta(\bar{t}+1) \equiv \eta(\bar{t})$. The value $\lfloor\bar{t}\rfloor = k$, $k = 0, 1, 2, \ldots$ is the normalized discrete time variable.

Eventually, integrating Eq. (2) over one ramp period one obtains the *primary stroboscopic mapping* given by the following non-autonomous 1D piecewise-smooth map

$$x_{k+1} = F(x_k, k), \tag{3a}$$

$$F(x,k) = \begin{cases} F_{\mathcal{L}}(x,k) = bx - b + 1 & \text{if } x \in \mathcal{I}_{\mathcal{L}}; \\ F_{\mathcal{M}}(x,k) = bx - b - 1 + 2b^{1-z(x,k)} & \text{if } x \in \mathcal{I}_{\mathcal{M}}; \\ F_{\mathcal{R}}(x,k) = bx + b - 1 & \text{if } x \in \mathcal{I}_{\mathcal{R}}, \end{cases} \tag{3b}$$

with $b = e^{\lambda}$, $\lambda < 0$. Here the partitions

$$\begin{aligned} \mathcal{I}_{\mathcal{L}} &= \{(x,k) \mid x \leqslant s^-(k)\}, \\ \mathcal{I}_{\mathcal{M}} &= \{(x,k) \mid s^-(k) < x < s^+(k)\}, \\ \mathcal{I}_{\mathcal{R}} &= \{(x,k) \mid x \geqslant s^+(k)\} \end{aligned} \tag{3c}$$

are separated from each other by the borders

$$s^{\pm}(k) = \left\{(x,k) \mid x = \frac{q}{\Gamma}\cos\left(\frac{2\pi k}{m}\right) \pm \frac{P}{\alpha\Gamma}\right\} \tag{3d}$$

and the function

$$z(x,k) = \frac{\alpha q}{2P}\cos\left(\frac{2\pi k}{m}\right) - \frac{\alpha\Gamma}{2P}x + \frac{1}{2} \tag{3e}$$

with $0 \leqslant z(x,k) \leqslant 1$ reflects the pulse duration in the operating regime without saturation, normalized with respect to the ramp period a.

2.2. *Unipolar H-bridge inverter*

The second model describes the behavior of the considered unipolar single-phase pulse-width modulated H-bridge inverter shown schematically in Fig. 2(a). The generation of the control signals $K_F^+(t)$ and $K_F^-(t)$ used to control the four switches $S_1 - S_4$ of the inverter is illustrated in Figs. 2(b) and 3. By contrast to the bipolar modulation approach, unipolar pulse-width modulation technique uses two ramp signals $V_{\text{ramp}}(t)$ and $-V_{\text{ramp}}(t)$, driven by the same clock, but with opposite polarity. Thus, the AC output voltage V_{out} can take one of the three values, E_0, $-E_0$ and zero [Rashid & Luo, 2006].
The AC output voltage V_{out} is generated from the DC voltage E_0 as

$$V_{\text{out}} = \tfrac{1}{2}E_0\left(K_F^+(t) + K_F^-(t)\right).$$

Closer examination of Fig. 2(b) shows that the output voltage V_{out} switches between 0 and $+E_0$ if the control voltage $V_{\text{con}}(t)$ is positive, and between 0 and $-E_0$ if $V_{\text{con}}(t)$ is negative.

The dynamics of the inverter described above can be represented by the following non-autonomous differential equation with a discontinuous right hand side:

$$L\frac{di}{dt} = -R\,i + \tfrac{1}{2}E_0\left(K_F^+(t) + K_F^-(t)\right) \tag{4a}$$

with

$$\mathrm{K}_\mathrm{F}^+ = \begin{cases} +1 & \text{if } V_{\text{con}} \geqslant V_{\text{ramp}}(t), \\ -1 & \text{if } V_{\text{con}} < V_{\text{ramp}}(t), \end{cases} \tag{4b}$$

$$\mathrm{K}_\mathrm{F}^- = \begin{cases} +1 & \text{if } V_{\text{con}} \geqslant -V_{\text{ramp}}(t), \\ -1 & \text{if } V_{\text{con}} < -V_{\text{ramp}}(t), \end{cases} \tag{4c}$$

and

$$V_{\text{ramp}}(t) = V_0\left(t/a - \lfloor t/a \rfloor - \tfrac{1}{2}\right). \tag{4d}$$

Here the functions V_{con} and $V_{\text{ref}}(t)$ are as given by Eqs. (1c) and (1e), respectively.

Similar to the previous model described in Sec. 2.1, we can rewrite Eq. (4a) using dimensionless state x and time $\bar{t}$ variables as well as the normalized parameters P, q, λ, and Γ. Then, integrating the resulting model over one ramp period, we obtain the following non-autonomous 1D piecewise-smooth map:

$$x_{k+1} = F(x_k, k), \tag{5a}$$

$$F(x,k) = \begin{cases} F_{\mathcal{L}}(x,k) = bx - b + 1 & \text{if } x \in \mathcal{I}_{\mathcal{L}}; \\ F_{\mathcal{M}}(x,k) = bx + b^{\frac{1-\theta(x,k)}{2}} & \\ \qquad\qquad - b^{\frac{1+\theta(x,k)}{2}} & \text{if } x \in \mathcal{I}_{\mathcal{M}}; \\ F_{\mathcal{R}}(x,k) = bx + b - 1 & \text{if } x \in \mathcal{I}_{\mathcal{R}}, \end{cases} \tag{5b}$$

where the partitions $\mathcal{I}_{\mathcal{L}}$, $\mathcal{I}_{\mathcal{M}}$ and $\mathcal{I}_{\mathcal{R}}$ are defined by Eq. (3c) and separated from each other by the time-dependent boundaries $s^{\pm}(k)$ given by Eq. (3d). The function

$$\theta(x,k) = \frac{\alpha q}{P}\cos\left(\frac{2\pi k}{m}\right) - \frac{\alpha\Gamma}{P}x \tag{6}$$

with $|\theta(x,k)| < 1$ combines the durations of both positive and negative pulses normalized with respect to one ramp period (see Figs. 2(b) and 3). More precisely, if $0 < \theta(x,k) \leqslant 1$, then a positive pulse with the duration $z_k^+ = \theta(x,k)$ is applied, and if $-1 \leqslant \theta(x,k) < 0$, a negative pulse of the duration $z_k^- = -\theta(x,k)$. In other words, the duration of the pulses in both cases is given by $|\theta(x,k)|$, and the kind of the pulse (positive or negative) corresponds to the sign of $\theta(x,k)$. Note that the applied control produces positive pulses if $x_k > s_0(k)$ and negative pulses if $x_k < s_0(k)$, where

$$s_0(k) = \left\{(x,k) \mid x = \frac{q}{\Gamma}\cos\left(\frac{2\pi k}{m}\right)\right\}. \tag{7}$$

Nevertheless, the point $s_0(k)$ is not a border point in the model, because identical durations of positive and negative pulses imply that for each k the function $F_{\mathcal{M}}(x,k)$ is smooth in $s_0(k)$.

2.3. *Multi-level unipolar H-bridge inverter*

The third model describes the dynamics of the multi-level cascaded H-bridge inverter with a unipolar sinusoidal PWM [S.Khomfoi & Tolbert, 2011] shown schematically in Fig. 4. In such an inverter with N cells (two cascaded H-bridge inverter system) and $2N$ levels, the feedback control is implemented using $2N$ ramp signals. In the case $N = 2$, i.e., for a 4-level inverter, the model in continuous time is given by

$$L\frac{di}{dt} = -R\,i + \tfrac{1}{4}E_0\sum_{j=1}^{4}\mathrm{K}_\mathrm{F}^{(j)}, \tag{8a}$$

where

$$\mathrm{K}_{\mathrm{F}}^{(j)} = \begin{cases} +1 & \text{if} \quad V_{\text{con}} \geqslant V_{\text{ramp}}^{(j)}, \\ -1 & \text{if} \quad V_{\text{con}} < V_{\text{ramp}}^{(j)}, \end{cases} \tag{8b}$$

with $j = 1, 2, 3, 4$ and

$$V_{\text{ramp}}^{(1)} = V_0 \left(t/a - \lfloor t/a \rfloor - 1 \right), \tag{8c}$$
$$V_{\text{ramp}}^{(2)} = V_0 \left(-t/a + \lfloor t/a \rfloor \right), \tag{8d}$$
$$V_{\text{ramp}}^{(3)} = V_0 \left(t/a - \lfloor t/a \rfloor \right), \tag{8e}$$
$$V_{\text{ramp}}^{(4)} = V_0 \left(1 - t/a + \lfloor t/a \rfloor \right). \tag{8f}$$

Here, similar to the previous cases, the functions V_{con} and $V_{\text{ref}}(t)$ are as given by Eqs. (1c) and (1e), respectively.
This model leads to the following non-autonomous 1D piecewise-smooth map:

$$x_{k+1} = F(x_k, k), \tag{9a}$$

$$F(x,k) = \begin{cases} F_{\mathcal{L}}(x) = b(x-1)+1 \quad \text{if} \quad x \in \mathcal{I}_{\mathcal{L}}; \\ F_{\mathcal{M}}^{(1)}(x,k) = b(x-1) + \frac{1}{2} b^{1-z(x,k)} + \frac{1}{2} \\ \qquad \text{if} \quad x \in \mathcal{I}_{\mathcal{M}}^{(1)}; \\ F_{\mathcal{M}}^{(2)}(x,k) = b(x-\frac{1}{2}) + \frac{1}{2} b^{1-z(x,k)} \\ \qquad \text{if} \quad x \in \mathcal{I}_{\mathcal{M}}^{(2)}; \\ F_{\mathcal{M}}^{(3)}(x,k) = b(x+\frac{1}{2}) - \frac{1}{2} b^{1-z(x,k)} \\ \qquad \text{if} \quad x \in \mathcal{I}_{\mathcal{M}}^{(3)}; \\ F_{\mathcal{M}}^{(4)}(x,k) = b(x+1) - \frac{1}{2} b^{1-z(x,k)} - \frac{1}{2} \\ \qquad \text{if} \quad x \in \mathcal{I}_{\mathcal{M}}^{(4)}; \\ F_{\mathcal{R}}(x) = b(x+1)-1 \quad \text{if} \quad x \in \mathcal{I}_{\mathcal{R}}, \end{cases} \tag{9b}$$

As in the previous case, the function

$$z(x,k) = \begin{cases} \varphi(x,k) - 1 & \text{if} \quad x \in \mathcal{I}_{\mathcal{M}}^{(1)}, \\ \varphi(x,k) & \text{if} \quad x \in \mathcal{I}_{\mathcal{M}}^{(2)}, \\ -\varphi(x,k) & \text{if} \quad x \in \mathcal{I}_{\mathcal{M}}^{(3)}, \\ -\varphi(x,k) - 1 & \text{if} \quad x \in \mathcal{I}_{\mathcal{M}}^{(4)}, \end{cases} \tag{9c}$$

$$\varphi(x,k) = \frac{2\alpha q}{P} \cos\left(\frac{2\pi k}{m}\right) - \frac{2\alpha\Gamma}{P} x \tag{9d}$$

takes the values between zero and one and determines the duration of pulses in the operating regime without saturation, normalized with respect to parameter a. The outer partitions $\mathcal{I}_{\mathcal{L}}$, $\mathcal{I}_{\mathcal{R}}$ are defined by Eq. (3c) and the middle partition $\mathcal{I}_{\mathcal{M}}$ is subdivided into sub-partitions

$$\begin{aligned} \mathcal{I}_{\mathcal{M}}^{(1)} &= \{(x,k) \mid s^-(k) < x < s_{\mathcal{M}}^-(k)\}, \\ \mathcal{I}_{\mathcal{M}}^{(2)} &= \{(x,k) \mid s_{\mathcal{M}}^-(k) < x < s^0(k)\}, \\ \mathcal{I}_{\mathcal{M}}^{(3)} &= \{(x,k) \mid s^0(k) < x < s_{\mathcal{M}}^+(k)\}, \\ \mathcal{I}_{\mathcal{M}}^{(4)} &= \{(x,k) \mid s_{\mathcal{M}}^+(k) < x < s^+(k)\} \end{aligned} \tag{9e}$$

which are separated from each other by the border $s^0(k)$ given by Eq. (7) and by the borders $s_{\mathcal{M}}^{\pm}(k)$:

$$s_{\mathcal{M}}^{\pm}(k) = \left\{ (x,k) \mid x = s^0(k) \pm \frac{1}{2} \cdot \frac{P}{\alpha\Gamma} \right\}. \tag{9f}$$

2.4. *Piecewise-linear map*

Comparing the functions $F(x,k)$ given by Eqs. (3b), (5b), and (9b), one can immediately recognize a number of striking similarities. Indeed, all three functions are defined on the same partitions $\mathcal{I}_{\mathcal{L}}$, $\mathcal{I}_{\mathcal{M}}$, $\mathcal{I}_{\mathcal{R}}$ (note that the functions (3b) and (5b) are smooth on these partitions, while the function (9b) is piecewise-smooth on $\mathcal{I}_{\mathcal{M}}$). Moreover, on the outer partitions $\mathcal{I}_{\mathcal{L}}$ and $\mathcal{I}_{\mathcal{R}}$ all three functions are identical and linear. In fact, the functions differ on the middle partition $\mathcal{I}_{\mathcal{M}}$ only, where they are nonlinear (see Fig. 5). Therefore, the question arises how these nonlinearities influence the bifurcation structures in the corresponding maps and what are generic bifurcation patterns determined by the overall structure of the map independently of particular nonlinearities. From the applied point of view, this question is of a particular interest, because the nonlinearity of the function on the middle partition is related to the applied control strategy and the modulation technique.

In order to identify the generic bifurcation patterns in the considered class of models which do not depend on particular nonlinearities in the definition of $F(x,k)$ on the middle partition, let us replace the function $F_{\mathcal{M}}(x,k)$ in Eqs. (3b), (5b), and (9b) by its linear approximation defined by the points $(s_k^-, F_{\mathcal{M}}(s_k^-, k))$ and $(s_k^+, F_{\mathcal{M}}(s_k^+, k))$. In this way, we obtain the following piecewise-linear map

$$x_{k+1} = F(x_k, k), \quad k = 0, 1, 2, ... \tag{10a}$$

$$F(x,k) = \begin{cases} F_{\mathcal{L}}(x) = bx - b + 1, & \text{if } x \in \mathcal{I}_{\mathcal{L}}; \\ F_{\mathcal{M}}(x,k) = c\,x + \theta(k), & \text{if } x \in \mathcal{I}_{\mathcal{M}}; \\ F_{\mathcal{R}}(x) = bx + b - 1, & \text{if } x \in \mathcal{I}_{\mathcal{R}}. \end{cases} \tag{10b}$$

$$c = b - \frac{\alpha\Gamma}{P}(1-b), \qquad \theta(k) = \mu \cos\left(\frac{2\pi\, k}{m}\right), \quad \mu = \frac{\alpha\, q\, (1-b)}{P}, \tag{10c}$$

As before, the partitions $\mathcal{I}_{\mathcal{L}}$, $\mathcal{I}_{\mathcal{M}}$, and $\mathcal{I}_{\mathcal{L}}$ are given by Eq. (3c). By definition, map (10) is non-autonomous, as the boundaries $s^{\mp}(k)$ between partitions $\mathcal{I}_{\mathcal{L}}$, $\mathcal{I}_{\mathcal{M}}$, $\mathcal{I}_{\mathcal{R}}$, and therefore (by continuity of the function) also the offset $\theta(k)$ of the function $F_{\mathcal{M}}$ depend explicitly on k. This is illustrated in Fig. 6, which shows the function F depending on x and k. As one can see, the slopes of the branches $F_{\mathcal{L}}(x,k^*)$, $F_{\mathcal{M}}(x,k^*)$, $F_{\mathcal{R}}(x,k^*)$ remain the same for any fixed k^*. What changes depending on k^*, is the position of the border points and the offset of the middle branch $F_{\mathcal{M}}(x,k^*)$.

Next, in order to obtain an autonomous model, we follow the same approach as in [Avrutin *et al.*, 2015, 2016, 2017b], and introduce the *secondary stroboscopic mapping* over one period of the low frequency signal. Since the frequency modulation ratio is assumed to be integer, this mapping is given by the m-th iterate of the primary stroboscopic mapping:

$$x_{n+1} = f_i^m(x_n) = F(\dots(F(F(x_n,i),(i+1) \bmod m),\dots),(i+m-1) \bmod m). \tag{11}$$

Note that, as the low frequency signal is m-periodic, for each $0 \leqslant i < m$, map (11) is autonomous. In the following, we investigate the dynamics of map (10) using the secondary stroboscopic map f_0^m, denoted simply by f^m. Clearly, an attracting m-cycle of map (10) corresponding to a desired working regime of the modeled inverter is associated in map (11) with an attracting fixed point.

Following a standard approach of symbolic dynamics, one can associate an orbit of map (10) with a symbolic sequence $\sigma = \sigma_0\sigma_1\sigma_2\dots$ with $\sigma_k \in \{\mathcal{L}, \mathcal{M}, \mathcal{R}\}$, $k \geqslant 0$. Each letter in this sequence is determined by the partition $\mathcal{I}_{\sigma_k}$ to which the corresponding point x_k belongs. As usual, we associate an m-cycle of map (10) with a shift-invariant symbolic sequence σ of length m. In the following, this cycle is denoted by $\mathcal{O}_\sigma$. Clearly, the same symbolic sequence σ is associated also with the corresponding fixed point of map (11). For example, if an m-cycle of map (10) is completely located inside the middle partition $\mathcal{I}_{\mathcal{M}}$ (see below, Fig. 7(a)), both this cycle and the corresponding fixed point of map (11) are associated with the symbolic sequence $\mathcal{M}^m$.

To characterize cycles of map (10), we consider below the ratios of particular letters in the associated symbolic sequences. For a symbolic sequence σ consisting of $N_{\mathcal{L}}(\sigma)$, $N_{\mathcal{M}}(\sigma)$, and $N_{\mathcal{R}}(\sigma)$ letters $\mathcal{L}$, $\mathcal{M}$, $\mathcal{R}$, respectively, with $N_{\mathcal{L}}(\sigma)+N_{\mathcal{M}}(\sigma)+N_{\mathcal{R}}(\sigma) = m$, these ratios are defined by

$$\rho_{\mathcal{C}}(\sigma) = \frac{N_{\mathcal{C}}(\sigma)}{m}, \quad \mathcal{C} \in \{\mathcal{L}, \mathcal{M}, \mathcal{R}\} \tag{12}$$

As an example, for the cycle $\mathcal{O}_\sigma$ with $\sigma = \mathcal{M}^{28}\mathcal{L}^{22}\mathcal{M}^{28}\mathcal{R}^{22}$ shown in Fig. 7(b) these ratios are given by $\rho_{\mathcal{L}}(\sigma) = 0.22$, $\rho_{\mathcal{M}}(\sigma) = 0.56$, and $\rho_{\mathcal{R}}(\sigma) = 0.22$.

3. Bifurcation structures

In the following, we consider the bifurcation structure of the (α, Γ) parameter plane of map (10), $0.0 < \Gamma < 60.0$, $\alpha > 0.0$ at the parameter values $\lambda = -0.2$, $q = 40.0$, $P = 20.0$, which correspond to physical implementations of the inverters described in Sec. 2.1 – 2.3. As follows from the results obtained before for other models, we have also distinguish between odd and even values of the frequency modulation ratio m. Here, as typical values we consider $m = 100$ and $m = 101$.

3.1. *Domains* $\Pi_1^{(1)}$, $\Pi_1^{(4)}$ *and* $\Pi_1^{(*)}$

As one can see in Fig. 8, the major part of the (α, Γ) parameter plain of map (11) is covered by the domain Π_1 corresponding to stable and globally attracting fixed points of map (11), and by the domain Π_∞ where map (11) has chaotic attractors. Similar to the nonlinear models considered in [Avrutin *et al.*, 2015, 2016, 2017b], the boundary has a quite frayed and irregular shape, so that one can conclude that this irregularity is not caused by the nonlinearities of the models considered in the cited works. Remarkably, for smaller values of Γ (in the lower part of Fig. 8(a)), the boundary between the domains Π_1 and Π_∞ has a complex oscillating shape, as illustrated in the magnifications shown in Figs. 8(b),(c),(d). It can also clearly be seen that this oscillating part of the boundary converges to a particular point, above which the shape of the boundary changes.

To explain the observed properties of the boundary between the domains Π_1 and Π_∞, it is necessary to consider the interior structure of Π_1. Recall that each fixed point of map (11) corresponds to an m-cycle of map (10) and is associated with a symbolic sequence σ of length m. According to the symbolic sequences associated with the fixed points of map (11), the following three sub-regions of the region Π_1 can be identified: .

$\Pi_1^{(1)}$: in this region, the complete cycle is located in the middle partition, so that the symbolic sequence associated with the cycle is $\mathcal{M}^m$. This corresponds to the working regime of the modeled inverter without saturation.

$\Pi_1^{(4)}$: in this region, the symbolic sequence associated with the cycle consists of four blocks consisting of the same letters and is of the form $\mathcal{M}^{n_1}\mathcal{L}^{n_2}\mathcal{M}^{n_3}\mathcal{R}^{n_4}$, $n_1 + n_2 + n_3 + n_4 = m$, $n_i > 0$, $i = 1, 2, 3, 4$. Accordingly, the modeled inverter is saturated twice per period of the low frequency reference signal, once from above and once from below. Note that the region Π_1^4 has a regular interior structure which differs for odd and even values of m (see Sec. 3.2).

$\Pi_1^{(*)}$: In this region, the modulator is saturated more than once per period from each side and the symbolic sequence associated with the cycles consist of more than four blocks. In the parameter space, the region Π_1^* is located between the region Π_1^4 and the chaotic domain Π_∞. It has a complicated interior structure which is reflected in the oscillating shape of the boundary between regular and chaotic domains.

A similar partitioning of the region Π_1 into the subdomains $\Pi_1^{(1)}$, $\Pi_1^{(4)}$ and $\Pi_1^{(*)}$ has been reported for the first time in [Avrutin *et al.*, 2015] for map (3). The present results confirm that this structure has a more general meaning and can be expected in all models leading to the piecewise-linear approximation given by map (10).

Note that, although in all three regions the map (11) has globally attracting stable fixed points, the properties of the corresponding m-cycles of map (10) differ. Indeed, fast-scale oscillations may lead to a significant distortion of cycles of map (10) which are not reflected in the corresponding fixed points of map (11). To illustrate this, Fig. 7 shows the typical shapes of m-cycles of map (10) for parameter values in the regions $\Pi_1^{(1)}$, $\Pi_1^{(4)}$ and $\Pi_1^{(*)}$. As one can see in Fig. 7(a), the cycles existing in the domain $\Pi_1^{(1)}$ are sufficiently smooth (being confined in a narrow band between two smooth boundaries $s_k^\pm$). Since the smoothness of the output signal of the inverter (reflected in low values of its total harmonic distortion) is an important issue for its practical use, the region $\Pi_1^{(1)}$ corresponds to the optimal operation mode of the circuit. In the region $\Pi_1^{(4)}$ (Fig. 7(b)), the signal is less smooth, first due to the kinks at the borders $s_k^\pm$ between the middle and the outer partitions, and second due to the flat plateaus in the outer partitions. Accordingly, the quality of the output signal of the inverter in the region $\Pi_1^{(4)}$ is considerably lower than in $\Pi_1^{(1)}$ and, as shown below, decreases for decreasing Γ. Still, the harmonic distortion of the signals in the region $\Pi_1^{(4)}$ is still much lower than in the region $\Pi_1^{(*)}$. Indeed, in that region a third factor appears which decreases the quality of the output signal, namely, fast-scale oscillations, similar to the bubbling phenomenon [Avrutin *et al.*, 2017a]. As one can see in Fig. 7(b), in the presented case these oscillations are already sufficiently strong to force the cycle to jump from one of the outer partitions into the other one. Although the mechanism leading to the appearance of these fast-scale oscillations is still not completely understood, their presence in the piecewise-linear map (10) demonstrates that they are not related to the nonlinearities of the particular models where they were observed before.

3.2. *Border collisions*

The lower boundary of the region Π_1^1 corresponds to a border collision $\xi_{\mathcal{M}^m}$ at which a point the cycle crosses one of the boundaries $s_k^\mp$ and enters thereafter into one of the outer partitions. A transition across this boundary (for decreasing values of Γ) is illustrated in Fig. 9. Note that at the moment of the border collision neither the periodicity nor the stability of any invariant set of map (10) changes, the topological structure of the phase space remains the same, so that the border collision (frequency referred to as a persistence border collision) can hardly be classified as a bifurcation. What changes at the moment of a persistence border collision bifurcation is the location of the cycle with respect to the partitions' boundaries, and therefore also the ratios of the letters in the associated symbolic sequences. As one can see in Fig. 9(c),(d), the ratio $\rho_{\mathcal{M}}$ (which is by definition 1.0 in the region $\Pi_1^{(1)}$) decreases monotonously with decreasing Γ. Accordingly, the ratios $\rho_{\mathcal{L}}$ and $\rho_{\mathcal{R}}$ increase (since, by definition, $\rho_{\mathcal{L}}+\rho_{\mathcal{M}}+\rho_{\mathcal{R}}=1$), which means for the output signal of the inverter that the the length of the plateaus in the outer partitions increases and the quality of the signal decreases monotonously with decreasing Γ.

The interior structure of the domain $\Pi_1^{(4)}$ is organized by a grid-like structure formed by persistence border collision boundaries, as illustrated in Figs. 10 and 11. As one can see, the structures for odd and even values of the frequency modulation ratio m differ in size of the grid step. To understand the reasons for that, let us consider how the symbolic sequences associated with the cycles and the values $\rho_{\mathcal{M}}$ change as the parameters are varied across this grid. It can easily be seen in Fig. 9(d) that for an odd value of m this value changes by $\frac{1}{m}$ at each border collision event. Indeed, as the boundary $\xi_{m^{101}}$ is crossed, we observe (for decreasing Γ) the sequence of cycles

$$\begin{aligned}\mathcal{O}_{\mathcal{M}^{101}} &\to \mathcal{O}_{\mathcal{M}^{100}\mathcal{L}} \to \mathcal{O}_{\mathcal{M}^{49}\mathcal{R}\mathcal{M}^{50}\mathcal{L}} \\ &\to \mathcal{O}_{\mathcal{M}^{49}\mathcal{R}\mathcal{M}^{49}\mathcal{L}^2} \to \mathcal{O}_{\mathcal{M}^{48}\mathcal{R}^2\mathcal{M}^{49}\mathcal{L}^2} \\ &\to \mathcal{O}_{\mathcal{M}^{48}\mathcal{R}^2\mathcal{M}^{48}\mathcal{L}^3} \to \dots\end{aligned} \tag{13}$$

In other words, at the moment of the first border collision the cycle $\mathcal{O}_{\mathcal{M}^{101}}$ touches the boundary s_k^- for some $k=k^*$, which leads to the appearance of the cycle $\mathcal{O}_{\mathcal{M}^{100}\mathcal{L}}$ after this border collision event. For decreasing Γ this cycle continue to grow and reaches the boundary s_k^+ at $k=k^*+50$, so that the cycle after the border collision becomes $\mathcal{O}_{\mathcal{M}^{49}\mathcal{R}\mathcal{M}^{50}\mathcal{L}}$. The process continues in a similar way, preserving the symmetry of the cycles as much as possible for cycles of odd length, so that each cycles involved in this structure is associated either with a symbolic sequence

$$\mathcal{M}^{\frac{m-1}{2}-\ell}\mathcal{R}^{\ell}\mathcal{M}^{\frac{m-1}{2}-\ell}\mathcal{L}^{\ell+1} \tag{14}$$

or with

$$\mathcal{M}^{\frac{m-1}{2}-\ell-1}\mathcal{R}^{\ell}\mathcal{M}^{\frac{m-1}{2}-\ell}\mathcal{L}^{\ell}, \tag{15}$$

where $\ell=0,\dots,(\frac{m-1}{2}-1)$. Accordingly, each cell in the overall grid-like structure is the existence region of a cycles associated with a symbolic sequence (14) or (14). Such a cell has a rhomboid shape and is confined by four persistence border collision curves, and the symbolic sequences in the adjacent cells differ by one in the number of the letters $\mathcal{L}$ or $\mathcal{R}$. The corner points of the cells correspond to codimension-2 border collision events, at which two points of the cycle collide with the boundaries simultaneously, one with $s_{k_1}^+$ and the other one with $s_{k_2}^+$.

As one can see in Fig. 10, for even values of m the cells of the grid-like structure in the domain $\Pi_1^{(4)}$ are about twice as big as for odd m. Moreover, Fig. 9(c) suggests that at each border collision event the value $\rho_{\mathcal{M}}$ changes by $\frac{2}{m}$, which seems to contradict the fact that the grid-like structure is formed by codimension-1 persistence border collision boundaries.

To explain this effect, let us consider first the cycle $\mathcal{O}_{\mathcal{M}^m}$ with an even m. In fact, for other cycles the calculations similar to the ones presented below are possible as well, but are quite tedious. Recall that for each $k=0,\dots,m-1$ the branch $F_{\mathcal{M}}$ of the function F has the same slope c and a different offset $\theta(k)$. Accordingly, starting with $k=0$, we obtain

$$x_1 = c\,x_0+\theta(0), \tag{16a}$$

$$x_2 = c^2\,x_0+c\,\theta(0)+\theta(1), \tag{16b}$$

$$x_3 = c^3\,x_0+c^2\,\theta(0)+c\,\theta(1)+\theta(2), \tag{16c}$$

$$\dots$$

$$\begin{aligned}x_k &= c^k\,x_0+\sum_{i=1}^{k}c^{k-i}\,\theta(i-1) \\ &= c^k\,x_0+\mu\sum_{i=1}^{k}c^{k-i}\,\cos\left(\frac{2\pi\,(i-1)}{m}\right).\end{aligned} \tag{16d}$$

Using Eq. (16d), we obtain for $k=m$:

$$x_m = c^m\,x_0+\mu\sum_{i=1}^{m}c^{m-i}\,\cos\left(\frac{2\pi\,(i-1)}{m}\right).$$

Then, the periodicity condition $x_0=x_m$ implies

$$x_0 = c^m\,x_0+\mu\sum_{i=1}^{m}c^{m-i}\,\cos\left(\frac{2\pi\,(i-1)}{m}\right). \tag{17}$$

Solving Eq. (17) with respect to x_0, we obtain the starting point of the cycle $\mathcal{O}_{\mathcal{M}^m}$:

$$x_0 = \frac{\mu}{1-c^m}\sum_{i=1}^{m}c^{m-i}\,\cos\left(\frac{2\pi\,(i-1)}{m}\right). \tag{18}$$

Finally, substituting the expression (18) for x_0 into Eq. (16d) we obtain all the points x_k,

$k = 0, \ldots, m-1$ of the cycle $\mathcal{O}_{\mathcal{M}^m}$:

$$x_k = \frac{\mu}{1-c^m} \sum_{i=1}^{m} c^{m+k-i} \cos\left(\frac{2\pi\,(i-1)}{m}\right) + \mu \sum_{i=1}^{k} c^{k-i} \cos\left(\frac{2\pi\,(i-1)}{m}\right). \tag{19}$$

Using Eq. (19), one can demonstrate that for even values of m the points of the cycle $\mathcal{O}_{\mathcal{M}^m}$ fulfill the following symmetry property:

$$x_{k+\frac{m}{2}} = -x_k, \quad k = 0, \ldots, \tfrac{m}{2}-1. \tag{20}$$

(for the proof see Appendix A). Note also that the same symmetry property is fulfilled also by the boundaries $s_k^{\pm}$:

$$s^{\pm}_{k+\frac{m}{2}} = -s^{\mp}_k, \quad k = 0, \ldots, \tfrac{m}{2}-1. \tag{21}$$

Therefore, when for some $k = k^*$ the point x_k of the cycle $\mathcal{O}_{\mathcal{M}^m}$ touches the boundary s_k^+, the point $x_{k+\frac{m}{2}}$ touches the boundary $s^+_{k+\frac{m}{2}}$, so that the cycle after this border collision is $\mathcal{O}_{\mathcal{M}^{\frac{m}{2}-1}\mathcal{R}\mathcal{M}^{\frac{m}{2}-1}\mathcal{L}}$. Moreover, the symmetry property (20) applies not only to the cycle $\mathcal{O}_{\mathcal{M}^m}$, so that each cycle in the domain $\Pi_1^{(4)}$ for even values of m is associated with a symbolic sequence

$$\mathcal{M}^{\frac{m}{2}-\ell}\mathcal{R}^{\ell}\mathcal{M}^{\frac{m}{2}-\ell}\mathcal{L}^{\ell} \tag{22}$$

where $\ell = 0, \ldots, (\frac{m}{2}-1)$. For example, the sequence of the border collision events shown in Fig. 9(a) begins with the following cycles:

$$\begin{aligned} \mathcal{O}_{\mathcal{M}^{100}} &\to \mathcal{O}_{\mathcal{M}^{49}\mathcal{R}\mathcal{M}^{49}\mathcal{L}} \to \mathcal{O}_{\mathcal{M}^{48}\mathcal{R}^2\mathcal{M}^{48}\mathcal{L}^2} \\ &\to \mathcal{O}_{\mathcal{M}^{47}\mathcal{R}^3\mathcal{M}^{47}\mathcal{L}^3} \to \mathcal{O}_{\mathcal{M}^{46}\mathcal{R}^4\mathcal{M}^{46}\mathcal{L}^4} \\ &\to \mathcal{O}_{\mathcal{M}^{45}\mathcal{R}^5\mathcal{M}^{45}\mathcal{L}^5} \to \ldots \end{aligned} \tag{23}$$

This explains why in Fig. 9(c) the value $\rho_{\mathcal{M}}$ changes by $\frac{2}{m}$ at each border collision event.

Note that the presented symmetry property of the grid-like structure in the domain $\Pi_1^{(4)}$ for even values of m is a peculiarity of the piecewise-linear map (10). Indeed, a similar structure has been described for the first time in [Avrutin *et al.*, 2016] for map (3). For this map, which has a nonlinear branch $F_{\mathcal{M}}$, the border collision events at the upper and lower boundaries take place not simultaneously, although the corresponding border collision curves in the parameter space quite close to each other. As a consequence the cells of the grid corresponding to the cycles associated with the symbolic sequence which are not of the form given in (22) are significantly smaller than the other cells. Evidently, as the branch $F_{\mathcal{M}}$ approaches its linear approximation, the size of such cells tends to zero, and their disappearance the piecewise-linear map (10) can be seen as a kind of degeneration of a more complex structure existing in models with nonlinear branches.

Note that the described property applies not only to cycles of map (10) existing in the domain $\Pi_1^{(4)}$. In fact, the symmetry of the cycles for even values of the frequency modulation ratio m influences all structures involving border collisions. As an example, Figs. 12(a), (b) show transitions from the domain $\Pi_1^{(*)}$ to chaos via irregular cascades of border collisions (see [Avrutin *et al.*, 2015]). The structure appearing in the case $m = 101$ is evidently more complex than in the case $m = 100$. A similar transition to chaos from the domains $\Pi_{1,1}$ for $m = 100$ and Π_2 for $m = 101$ (see Sec. 3.3 for details) is illustrated in Figs. 12(c), (d). As a matter of fact, the complexity of the structure in the latter case is much higher.

3.3. *Degenerate pitchfork and flip bifurcations*

It has been reported in [Avrutin *et al.*, 2017b] that m-cycles of the nonlinear models considered in these works may undergo smooth pitchfork and flip bifurcations, which may be, depending on the particular system, super- or subcritical. In the piecewise-linear map (10) such bifurcations cannot occur. Instead, one can observe so-called degenerate pitchfork and flip bifurcations [Avrutin *et al.*, 2017b] which occur when the slope of a linear branch of map (11) containing a fixed point becomes ± 1.

More precisely, a degenerate pitchfork bifurcation is a special case of a so-called degenerate +1-bifurcation, as described in [Sushko & Gardini, 2010; Sushko *et al.*, 2016]. A stable fixed point $\mathcal{O}_\sigma$ of map (11) undergoes a degenerate pitchfork bifurcation if the eigenvalue $\Lambda(\mathcal{O}_\sigma)$ of $\mathcal{O}_\sigma$ passes through +1 and at the bifurcation moment the branch f_σ of the function f^m containing $\mathcal{O}_\sigma$ becomes the identity function. Accordingly, at the bifurcation moment map (10) has an interval filled with neutral (Lyapunov-stable, but not asymptotically stable) m-cycles. After this bifurcation, the map has two coexisting fixed points, which however – by contrast to a smooth pitchfork bifurcation – are not necessarily stable. If both of them are stable, their basins of attraction are separated from each other by the unstable fixed point $\mathcal{O}_\sigma$ and its preimages different form itself, if any exist. Otherwise, if one or both of them are unstable, the map may have chaotic

attractors (in particular, two coexisting chaotic attractors, or a chaotic attractor coexisting with a stable fixed point). One more difference to a smooth pitchfork bifurcation is that the fixed points appearing at a degenerate pitchfork bifurcation belong to the branches of the function adjacent to f_σ and are associated with symbolic sequences $\tilde{\sigma}$, $\hat{\sigma}$ complementary to σ. Moreover, as these fixed points appear from the end-points of the branch f_σ, the degenerate pitchfork bifurcation of $\mathcal{O}_\sigma$ corresponds to border collision bifurcations of $\mathcal{O}_{\tilde{\sigma}}$ and $\mathcal{O}_{\hat{\sigma}}$.
A supercritical degenerate flip bifurcation occurs similarly, with the difference that the eigenvalue $\Lambda(\mathcal{O}_\sigma)$ of $\mathcal{O}_\sigma$ passes through -1 and at the bifurcation moment the second iterate f_σ^2 of the branch f_σ becomes the identity function. Accordingly, at the bifurcation moment, each point of the branch f_σ except for $\mathcal{O}_\sigma$ belongs to a neutral 2-cycle, and after the bifurcation the map (11) has an attracting 2-cycle, appearing at the bifurcation moment via a border collision bifurcation.

Note that which particular bifurcation a cycle can undergo is directly determined by the symbolic sequence associated with the cycle. Indeed, the eigenvalue of the cycle $\mathcal{O}_\sigma$ is given by

$$\Lambda(\mathcal{O}_\sigma) = b^{N_{\mathcal{L}}(\sigma)}\, c^{N_{\mathcal{M}}(\sigma)}\, b^{N_{\mathcal{R}}(\sigma)}. \tag{24}$$

Since the slope b of the linear functions $F_{\mathcal{L}}$ and $F_{\mathcal{R}}$ is positive, and the slope c of $F_{\mathcal{M}}$ is negative, the eigenvalue $\Lambda(\mathcal{O}_\sigma)$ is positive for odd $N_{\mathcal{M}}(\sigma)$ and negative when $N_{\mathcal{M}}(\sigma)$ is even. Accordingly, in the former case the cycle $\mathcal{O}_\sigma$ can undergo a degenerate pitchfork and in the latter case a degenerate flip bifurcation. Moreover, as we have analytic expressions for the slopes b and c, Eq. (24) provides us with an analytic expression of the degenerate pitchfork or flip bifurcation curve for any cycle $\mathcal{O}_\sigma$. It follows also from Eq. (24) that these expressions are identical for any two cycles $\mathcal{O}_\sigma$ and $\mathcal{O}_\varrho$ with $N_{\mathcal{M}}(\sigma) = N_m(\varrho)$.

As an example, let us consider the fixed point $\mathcal{O}_{\mathcal{M}^m}$ which becomes unstable at the right boundary of the region $\Pi_1^{(1)}$ via a degenerate pitchfork bifurcation if m is even or via a degenerate flip bifurcation if m is odd. As all points of the cycle $\mathcal{O}_{\mathcal{M}^m}$ are located in the middle partition, Eq. (24) implies that its eigenvalue is given by

$$\Lambda(\mathcal{O}_{\mathcal{M}^m}) = \left(b - \frac{\alpha\Gamma}{P}(1-b)\right)^m \tag{25}$$

Combining this expression with the conditions of degenerate pitchfork and flip bifurcations

$$\Lambda(\mathcal{O}_{\mathcal{M}^m}) = +1 \quad \text{and} \quad \Lambda(\mathcal{O}_{\mathcal{M}^m}) = -1, \tag{26}$$

respectively, we obtain in both cases the following expression of the degenerate pitchfork or flip bifurcation curve

$$\psi_{\mathcal{M}^m} = \left\{(\alpha,\Gamma) \mid \Gamma = \frac{P}{\alpha}\cdot\frac{1+b}{1-b}\right\} \tag{27}$$

which confines the domain $\Pi_1^{(1)}$, as illustrated in Fig. 10.

For $m = 100$, a transition across the degenerate pitchfork bifurcation boundary $\psi_{\mathcal{M}^{100}}$ leading from the region $\Pi_1^{(1)}$ to the bistalility region $\Pi_{1,1}^{(1)}$, is illustrated in Figs. 13(a) and 14. As one can see in Fig. 14(a), after the bifurcation the fixed point $\mathcal{O}_{\mathcal{M}^m}$ has several preimages, so that the basins of attraction of the coexisting attractors (stable fixed points or chaotic attractors) has a structure shown in Fig. 14(b).
It is also visible in Fig. 14(a) that the branches of f^m containing the stable fixed appearing at the degenerate pitchfork bifurcation have very small domains. Therefore, for increasing values of α, the stable fixed points transits quickly from one branch to the next one. This results in two parallel cascades of persistence border collisions. The peculiarity of these cascades in the piecewise-linear map (11) with an even value of m is related to its symmetry. Indeed, the coexisting fixed points $\mathcal{O}_{\mathcal{M}^{99}\mathcal{L}}$ and $\mathcal{O}_{\mathcal{M}^{99}\mathcal{R}}$ appearing at the degenerate pitchfork bifurcation $\psi_{\mathcal{M}^{100}}$ are not symmetric for themselves, but symmetric to each other. As a consequence, with further increasing α, the fixed point $\mathcal{O}_{\mathcal{M}^{99}\mathcal{R}}$ collides with the boundary s_k^+ at the same moment as the fixed point $\mathcal{O}_{\mathcal{M}^{99}\mathcal{L}}$ collides with the boundary $s_{k+\frac{m}{2}}^+$.
After this persistence border collision event, the map has again two stable fixed points associated with symmetric symbolic sequences (recall that we call two symbolic sequences defined on the alphabet $\{\mathcal{L},\mathcal{M},\mathcal{R}\}$ symmetric if one of them results from the other one by interchanging the letters $\mathcal{L}$ and $\mathcal{R}$). Therefore, for increasing α, we observe a cascade of persistence border collisions, at each of which two coexisting cycles collide simultaneously with the opposite boundaries of the partition $\mathcal{I}_{\mathcal{M}}$. The first steps of this cascade, illustrated in the in-

set in Fig. 13(b), are

$$\begin{aligned}
&①\text{: } \mathcal{O}_{\mathcal{M}^{100}} \rightarrow \\
&②\text{: } (\mathcal{O}_{\mathcal{M}^{99}\mathcal{L}} \text{ and } \mathcal{O}_{\mathcal{M}^{99}\mathcal{R}}) \rightarrow \\
&③\text{: } (\mathcal{O}_{\mathcal{M}^{97}\mathcal{LML}} \text{ and } \mathcal{O}_{\mathcal{M}^{99}\mathcal{RMR}}) \rightarrow \\
&④\text{: } (\mathcal{O}_{\mathcal{M}^{46}\mathcal{LMLM}^{50}\mathcal{R}} \text{ and } \mathcal{O}_{\mathcal{M}^{46}\mathcal{RMRM}^{50}\mathcal{L}}) \rightarrow \\
&⑤\text{: } (\mathcal{O}_{\mathcal{M}^{46}\mathcal{LMLM}^{48}\mathcal{RMR}} \text{ and } \mathcal{O}_{\mathcal{M}^{46}\mathcal{RMRM}^{48}\mathcal{LML}}) \rightarrow \\
&⑥\text{: } (\mathcal{O}_{\mathcal{M}^{48}\mathcal{LMLM}^{48}\mathcal{R}} \text{ and } \mathcal{O}_{\mathcal{M}^{48}\mathcal{RMRM}^{48}\mathcal{L}}) \rightarrow \ldots
\end{aligned} \tag{28}$$

Here, the labels ① – ⑥ correspond to Fig. 13(b). Eq. (28) illustrates clearly the irregularity of this persistence border collision cascade. Indeed, the cycles collide with the boundaries at vastly different phases (see the transition ③ → ④), moreover, a point which has already entered one of the or the outer partitions $\mathcal{I}_{\mathcal{L}}$, $\mathcal{I}_{\mathcal{R}}$ may also move back to $\mathcal{I}_{\mathcal{M}}$. This explains why the ratio $\rho_{\mathcal{M}}$ in Fig. 13(b) decreases non-monotonously.

The structure formed by the coinciding border collision curves in the domain $\Pi_{1,1}^{(1)}$ is shown in Fig. 15. By contrast to the regular and well-understandable structure existing inside the domain $\Pi_1^{(4)}$, in the domain $\Pi_{1,1}^{(1)}$ no such simple regularities can be recognized. Indeed, Fig. 15 suggests that there are two different structures inside this domain. The first one, located in the lower part of Fig. 15 close to the boundary between $\Pi_{1,1}^{(1)}$ and $\Pi_1^{(1)}$ (see in the magnifications shown in Fig. 15(b)), is quite dense, white the second one located in the upper part of Fig. 15, is much less dense. This difference is reflected also in Fig. 13(a), where one can clearly see that the oscillations of the fixed points starting immediately after the degenerate pitchfork bifurcation $\psi_{\mathcal{M}^{100}}$ suddenly stop. However, at present the regularities behind these structures are still unclear. Note that in maps with nonlinear branches these structure becomes even more complex, since in these maps the coexisting fixed points do not undergo border collisions simultaneously.

For odd values of m, the overall bifurcation structure is quite similar to the one described above. As already mentioned, in this case the degenerate flip bifurcation curve $\psi_{\mathcal{M}^m}$ represents the boundary between the regions $\Pi_1^{(1)}$ associated with a globally attracting fixed point of map (11) and Π_2 associated with its globally attracting 2-cycle. Fig. 13(b) illustrates the transition across this boundary for $m = 101$. After the bifurcation, the cycle undergoes several persistence border collisions. In fact, in this case there are more border collisions than for even values of m, for the same reasons as the grid size in the region $\Pi_1^{(4)}$ is smaller for even than for odd m. This can be seen for example in the insets in Figs. 13(c) and 13(d), which magnify the same parameter interval for $m = 100$ and $m = 101$, respectively. It can also be seen in these figures that for $m = 101$ the ratio $\rho_{\mathcal{M}}$ is oscillating significantly stronger than for $m = 100$.

Clearly, not only the cycle $\mathcal{O}_{\mathcal{M}^m}$ but also other cycles may undergo degenerate pitchfork and flip bifurcations. As already mentioned in [Avrutin *et al.*, 2017b], it follows from Eq. (24) that for an m-cycle $\mathcal{O}_\sigma$ with j letters $\mathcal{M}$ in the associated symbolic sequence, $0 \leqslant j \leqslant m$, (and, accordingly, $m - j$ letters $\mathcal{L}$ and $\mathcal{R}$), the corresponding bifurcation boundary is given by

$$\psi_j = \left\{ (\alpha, \Gamma) \mid \Gamma = \frac{P}{\alpha} \cdot \frac{b^{1-\frac{m}{j}} + b}{1 - b} \right\}. \tag{29}$$

Obviously, Eq. (27) results from Eq. (29) for $j = m$. As before, if j is even, the curve ψ_j corresponds to a degenerate pitchfork, and if j is odd, to a degenerate flip bifurcation. Note that the not a particular symbolic sequence σ associated with a cycle is relevant here, but only the number $j = N_{\mathcal{M}}(\sigma)$. Accordingly, the curve ψ_j acts as a bifurcation boundary for all cycles with the same number j of points in the middle partition (provided, the cycle undergoes such a bifurcation). In the domain $\Pi_1^{(*)}$, this leads to the alignment of the bifurcation boundaries, as illustrated in Fig. 16. As one can see, this alignment is particularly well-visible is the parts of the boundary between the domains $\Pi_1^{(*)}$ and Π_∞, where degenerate pitchfork and flip bifurcations lead to the appearance of chaotic attractors. It is also clear that in the chaotic domain, close to its boundary given by a curve ψ_j with an even j, bistability in form of two coexisting chaotic attractors can be expected, while in the periodic domain, cycles with doubled period can be expected close to a curve ψ_j with an odd j.

In maps defined by functions with a nonlinear branch $F_{\mathcal{M}}$, a similar alignment may be present of not, depending on whether the branch is sufficiently close to its linear approximation. If for all $x \in \mathcal{I}_{\mathcal{M}}$ the value of the derivative $f'_{\mathcal{M}}$ is sufficiently close to c, the eigenvalue of all cycles with the same number j of points in the middle partition $\mathcal{I}_{\mathcal{M}}$ is sufficiently close to the value given by Eq. (24), independently on the location of the points of the cycle in $\mathcal{I}_{\mathcal{M}}$. In this case, all these cycles undergo smooth (not degenerate) pitchfork and flip bifurcations sufficiently close to the curve ψ^j. As discussed in [Avrutin *et al.*, 2017b], in map (5) the described alignment takes place, while in map (3) it does not. The reasons for that are clearly visible in Fig. 5: the maximal distance between the function $F_{\mathcal{M}}$ and its linear approximation in map (5) is smaller approximately by factor 100 than in map in map (3).

4. Summary

It is well known that models of power electronic converters belong to the scope of the theory of piecewise-smooth dynamical systems. It has been recently shown that DC/AC converters, whose dynamics is governed by two external signals with vastly different frequencies (a low frequency reference signal and a high frequency switching signal), lead to a specific class of piecewise-smooth maps. The characteristic feature of these maps is an extremely high (practically unpredictable) number of switching manifolds. As a matter of fact, bifurcation phenomena in such maps are not yet sufficiently understood. In particular, we have recently found that such maps may show several unusual effects, such as a transition from regular dynamics to chaos through an irregular sequence of persistence border-collisions [Avrutin *et al.*, 2015]; structures formed by border collision of persistence type occurring in the stability domain of fixed points [Avrutin *et al.*, 2016]; a global alignment of the bifurcation boundaries associated with smooth bifurcations [Avrutin *et al.*, 2017b]. However, the appearance of these effects has been demonstrated on several different models, while the question remained open which of them are related to particular nonlinearities of these models and which are more generic.

In order to provide an answer to this question, in the present paper we demonstrated how two common types of power electronic DC/AC converter systems, namely single-phase H-bridge and multi-level inverters can be examined by means of a piecewise-linear approximation. This map preserves the overall structure of particular approximated maps, neglecting the specific nonlinearities related to the applied feedback control. Due to the linearity of its branches, this map allows a more deep analytic treatment than the maps with non-linear branches. First, we have investigated the overall structure of the parameter space of the piecewise-linear map and have shown that the overall partitioning of the parameter space previously reported for several particular models has a generic character. Next, we have discussed bifurcation structures observed in a parameter plane of the piecewise-linear map, focusing on two types of events most characteristic for such maps, namely border collisions, which occur when a fixed point or cycle collides with a switching manifold in the state space, and bifurcations associated with the change of stability of a fixed point or cycle.

We have shown that in the case of an even frequency modulation ratio, the cycles of the piecewise-linear map possess a certain symmetry. This explains the differences in the structures formed by persistence border collisions for odd and even frequency modulation ratios, which have been previously reported not not understood. As a consequence of their symmetry, the cycles of the piecewise-linear map with an even frequency modulation ratio collide with the boundaries in the state space by two points simultaneously, which is not the case if the frequency modulation ratio is odd. Although in maps with nonlinear branches the symmetry is broken, it has still some consequences for these maps as well. In particular, the cycles which cannot occur in the piecewise-linear approximation (because they do not fulfill the symmetry) occur in maps with nonlinear branches in parameter regions which are significantly smaller than the existence regions of the cycles which occur in the piecewise-linear map.

The differences between odd and even values of the frequency modulation ratio m regards also the bifurcations related to the change of stability. In particular, the m-cycle of the piecewise-linear map (the fixed point of the secondary stroboscopic mapping) associated with the optimal operational regime of the modeled inverter without saturation becomes unstable via a degenerate pitchfork bifurcation if m is even and via a degenerate flip bifurcation if m is odd. As a consequence, for even values of m the stability region of this cycle in the parameter space is followed by the region of bistability.

Acknowledgments

The work of V. Avrutin was supported by the German Research Foundation within the scope of the project "Generic bifurcation structures in piecewise-smooth maps with extremely high number of borders in theory and applications for power converter systems".

Appendix A Proof of Eq. (20)

Eq. (19) can be rewritten as

$$\begin{aligned} x_k &= \frac{\mu}{1-c^m}\sum_{i=1}^{k} c^{k-i}\cos\left(\frac{2\pi\,(i-1)}{m}\right) + \\ &\quad \frac{\mu}{1-c^m}\sum_{i=k+1}^{m} c^{m+k-i}\cos\left(\frac{2\pi\,(i-1)}{m}\right) \\ &= \frac{\mu}{1-c^m}\,\phi_k \end{aligned} \tag{A.1}$$

where

$$\begin{aligned} \phi_k = &\sum_{i=1}^{k} c^{k-i}\cos\left(\frac{2\pi\,(i-1)}{m}\right) + \\ &\sum_{i=k+1}^{m} c^{m+k-i}\cos\left(\frac{2\pi\,(i-1)}{m}\right). \end{aligned} \tag{A.2}$$

or, equivalently,

$$\begin{aligned} \phi_k = &\sum_{i=0}^{k-1} c^{k-i-1}\cos\left(\frac{2\pi\,i}{m}\right) + \\ &\sum_{i=k}^{m-1} c^{m+k-i-1}\cos\left(\frac{2\pi\,i}{m}\right). \end{aligned} \tag{A.3}$$

After some algebraic transformations (e.g., using computer algebra software) one can show that

$$\begin{aligned} \phi_k = &\frac{-1}{(c+1)^2+4\,c\cos^2\left(\frac{\pi}{m}\right)}\Bigg((c^m-1)(c+1)- \\ &2\left(c^{m+1}+2c^m-c-1\right)\cos^2\left(\frac{\pi\,k}{m}\right)+ \\ &4\,(c^m-1)\cos^2\left(\frac{\pi\,k}{m}\right)\cos^2\left(\frac{\pi}{m}\right)+ \\ &(c^m-1)\sin\left(\frac{2\pi}{m}\right)\sin\left(\frac{2\pi\,k}{m}\right)+ \\ &2\cos^2\left(\frac{\pi}{m}\right)\Bigg) = A \end{aligned} \tag{A.4}$$

and moreover, that

$$\phi_{k+\frac{m}{2}} = -A \tag{A.5}$$

which means

$$\phi_k = -\phi_{k+\frac{m}{2}} \tag{A.6}$$

However, the expression $\phi_{k+\frac{m}{2}}$ is related to a point $x_{k+\frac{m}{2}}$ only if m is an even number. Accordingly, Eq. (A.6) proves Eq. (20), provided that m is even.

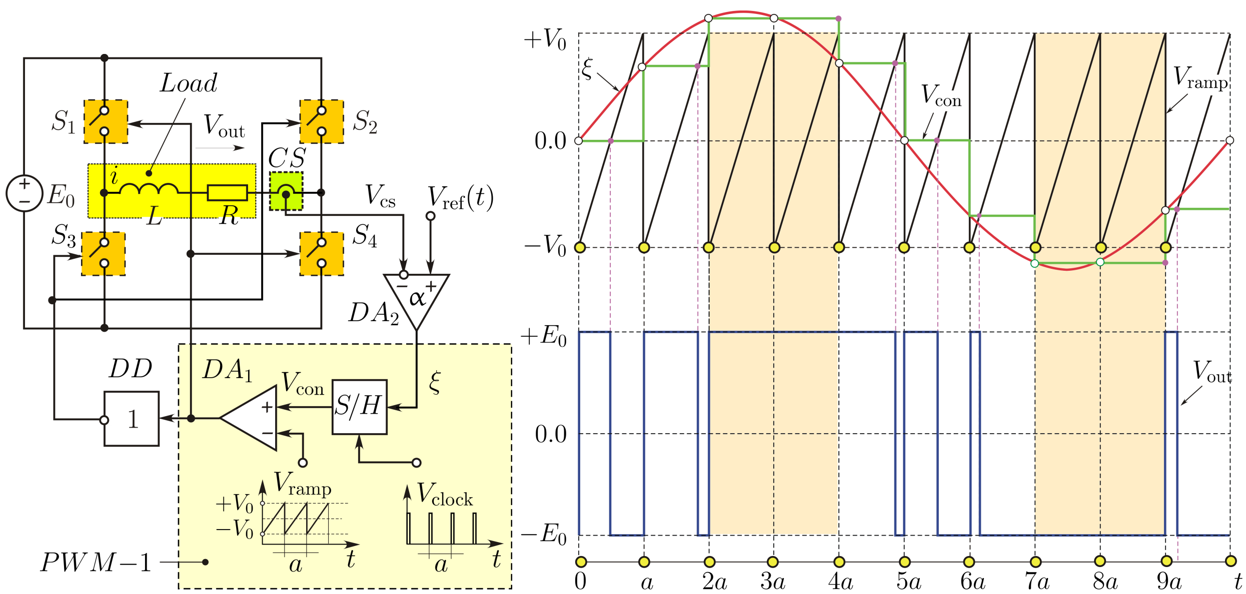

(a) (b)

Fig. 1. (a) Schematic diagram of the considered bipolar H-bridge inverter. E_0 is the externally supplied DC- voltage, and i is the AC-current supplied to the load. CS is the current sensor, $V_{\mathrm{ref}}(t) = V_m \cdot \cos(2\pi t/ma)$ the sinusoidal reference voltage, $V_{\mathrm{cs}}(t) = \beta i(t)$ is the output voltage of the current sensor, and $\xi(t) = \alpha(V_{\mathrm{ref}}(t) - \beta i(t))$ the amplified error signal. (b) Sketch of the current-mode control applied to generate the switching signals. The sample-and-hold unit S/H detects the sampled signal $\xi(ka)$ at the beginning of each clock time. This produces the control signal $V_{\mathrm{con}}(t)$ that together with the ramp function $V_{\mathrm{ramp}}(t)$ generates the red driving signals to the switches S_1, S_4, and S_2, S_3. The intervals $[2a, 4a)$ and $[7a, 9a)$ are related to saturation of the positive and the negative pulse, respectively.

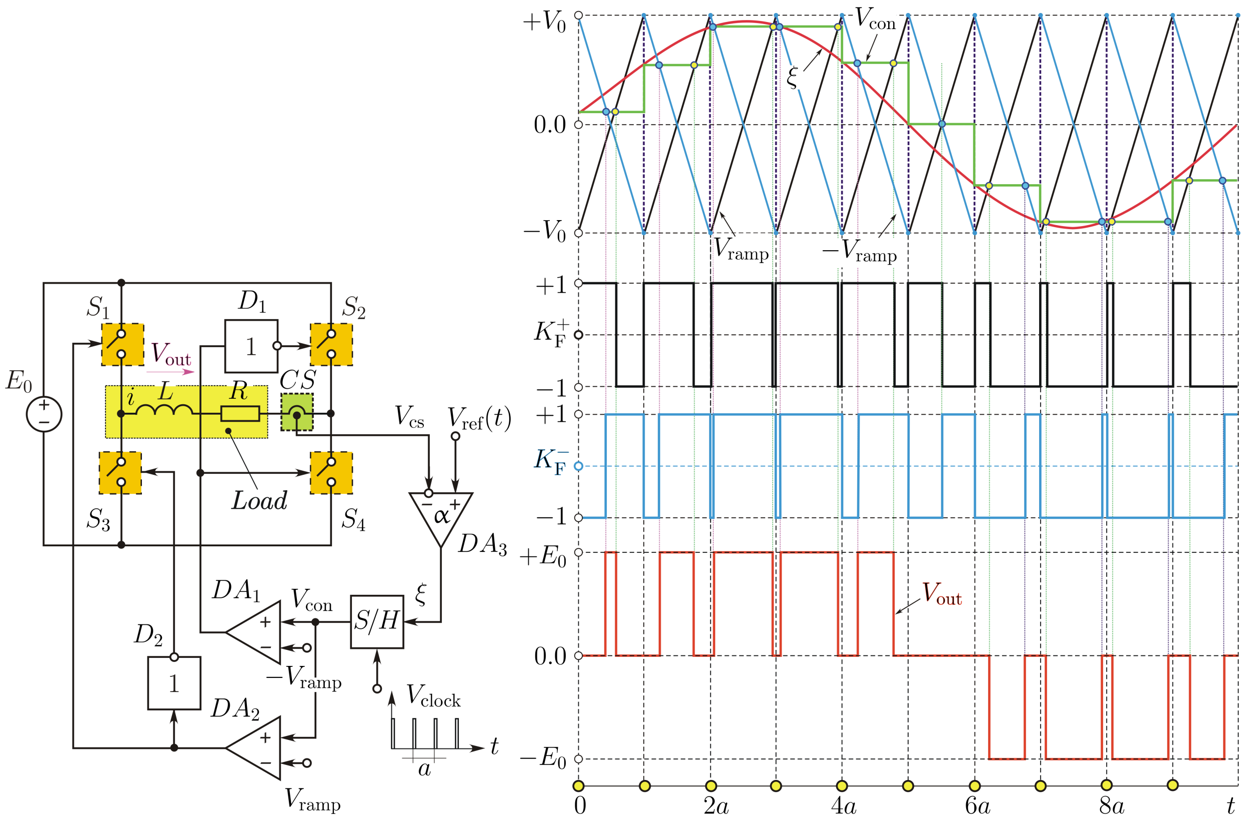

(a) (b)

Fig. 2. (a) Schematic diagram of the considered unipolar H-bridge inverter. (b) Time diagram illustrating the generation of the switching signals $\mathrm{K}_{\mathrm{F}}^{\pm}(t)$ and AC output voltage $V_{\mathrm{out}} = \frac{1}{2}E_0\left(\mathrm{K}_{\mathrm{F}}^{+} + \mathrm{K}_{\mathrm{F}}^{-}\right)$. If $V_{\mathrm{con}}(t) \geqslant V_0$ or $V_{\mathrm{con}}(t) \leqslant -V_0$, the modulator is saturated.

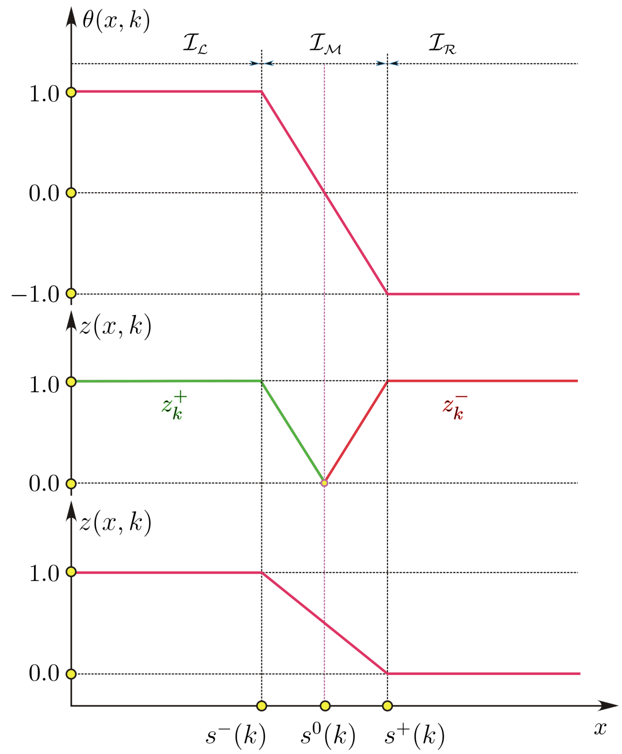

Fig. 3. Value $\theta(x,k)$ in three partitions $\mathcal{I}_\mathcal{L}$, $\mathcal{I}_\mathcal{M}$, $\mathcal{I}_\mathcal{R}$ (upper panel). Corresponding durations of positive and negative pulses z_k^+ / z_k^- in the unipolar PWM inverter modeled by map (5) (middle panel). Pulse duration z_k in bipolar PWM inverter modeled by map (3) (lower panel).

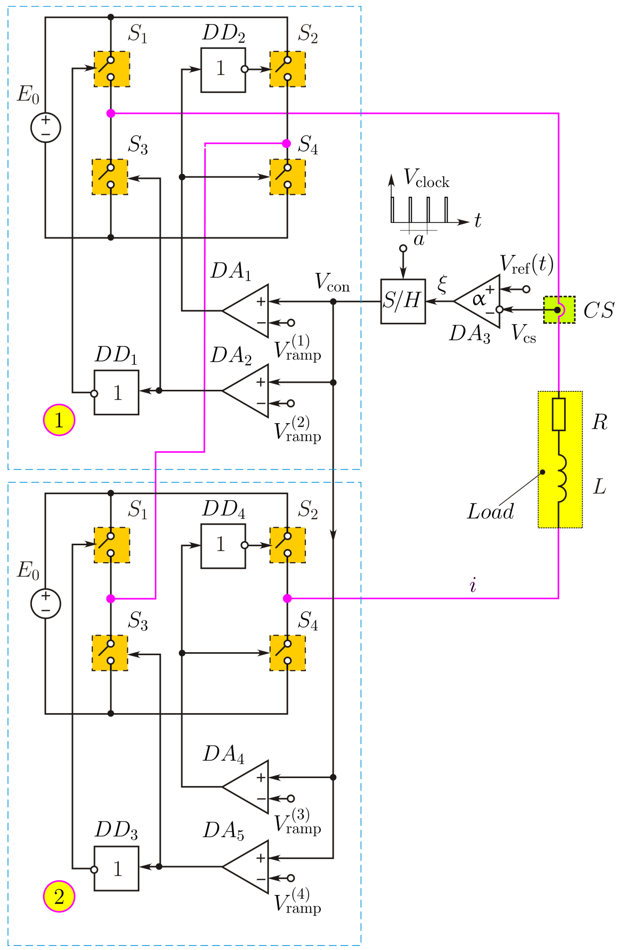

Fig. 4. Schematic diagram of the considered four-level cascaded H-bridge inverter with unipolar sinusoidal PWM-1. For the two cascaded H-bridge inverter systems, labeled by ① and ②, the feedback control is implemented using the four ramp signals $V^{(1)}_{\text{ramp}}$, $V^{(2)}_{\text{ramp}}$ and $V^{(3)}_{\text{ramp}}$, $V^{(4)}_{\text{ramp}}$.

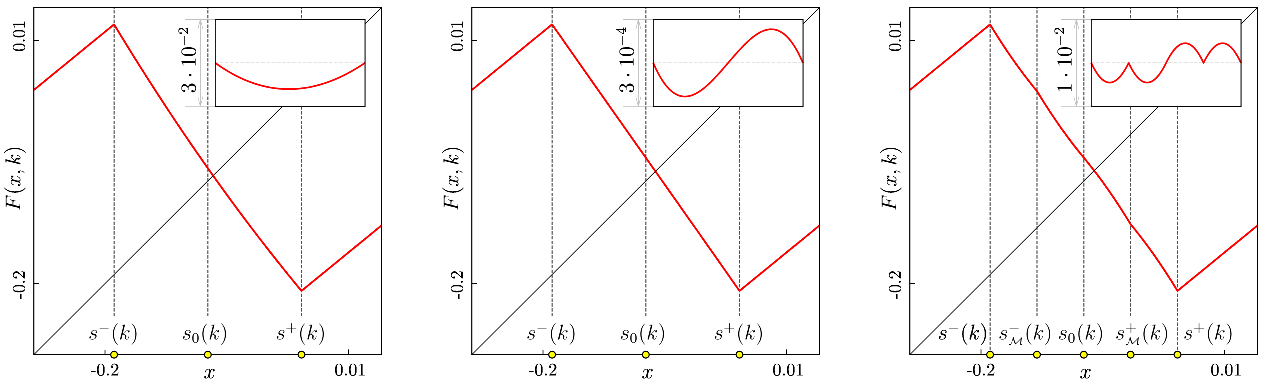

(a) (b) (c)

Fig. 5. Function $F(x,k)$ given by (a) Eq. (3b); (b) Eq. (5b); (c) Eq. (9b); for a fixed value $k = k^*$. The insets show the distance between $F(x, k^*)$ and its linear interpolation on the middle partitions $\mathcal{I}_\mathcal{M}$. $\alpha = 5.5$, $\Gamma = 45$, $m = 100$, $k^* = 27$.

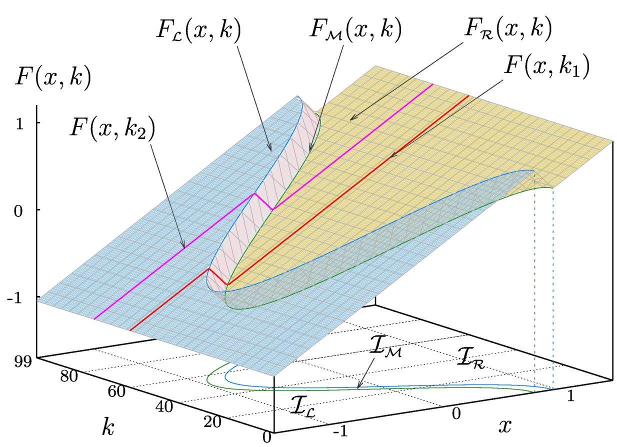

Fig. 6. Function $F(x,k)$ composed of the functions $F_\mathcal{L}(x,k)$, $F_\mathcal{M}(x,k)$ and $F_\mathcal{R}(x,k)$ which are linear both in x and k. Periodically oscillating boundaries $s_k^\pm$ are clearly visible (one period is shown). Two examples of the function $F(x,k)$ with a fixed k are presented (at $k_1 = 60$ and $k_2 = 75$). $\alpha = 5.5$, $\Gamma = 45.0$, $m = 100$.

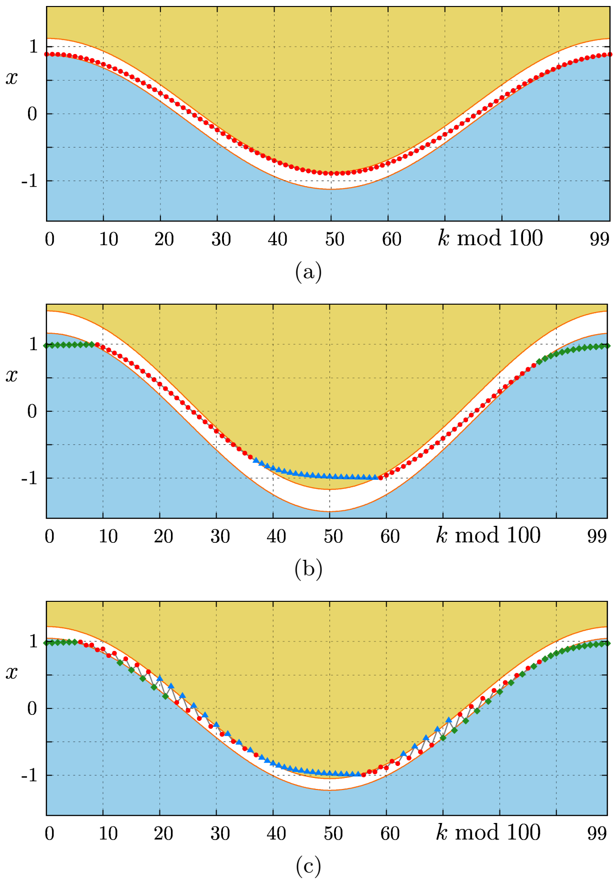

Fig. 7. Typical shapes of the m-cycles of map (10) for parameter values in the regions $\Pi_1^{(1)}$, $\Pi_1^{(4)}$ and $\Pi_1^{(*)}$, The presented cycles correspond to the symbolic sequences (a) $\mathcal{M}^{100}$, (b) $\mathcal{M}^{28}\mathcal{L}^{22}\mathcal{M}^{28}\mathcal{R}^{22}$, and (c) $\mathcal{M}^7(\mathcal{RM})^3(\mathcal{RL})^2(\mathcal{ML})^7\mathcal{ML}^{18}$ $\mathcal{M}^7(\mathcal{LM})^3(\mathcal{LR})^2(\mathcal{MR})^7\mathcal{MR}^{18}$. (a) $\alpha = 4.0$, $\Gamma = 40$; (b) $\alpha = 4.0$, $\Gamma = 30$; (c) $\alpha = 6.0$, $\Gamma = 35.22$; $m = 100$. The corresponding parameter values are marked in Fig. 10 with p_1, p_2, p_3, respectively.

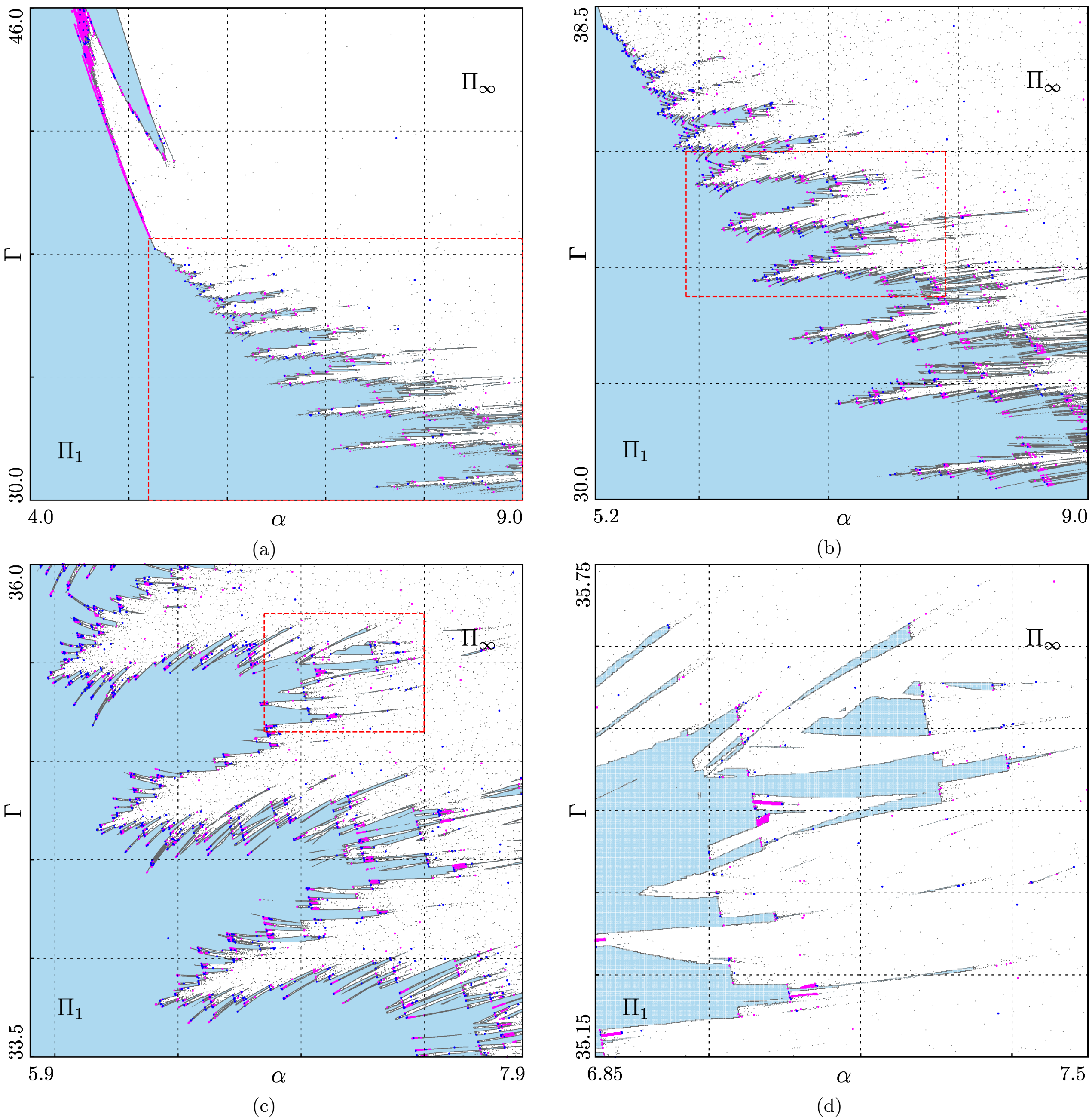

Fig. 8. Overall structure (a) of the (α, Γ) parameter plane of map (11) and its subsequent magnifications (b), (c), (d). Domains Π_1 and Π_∞ correspond to globally attracting stable fixed points and chaotic attractors, respectively. $m = 100$.

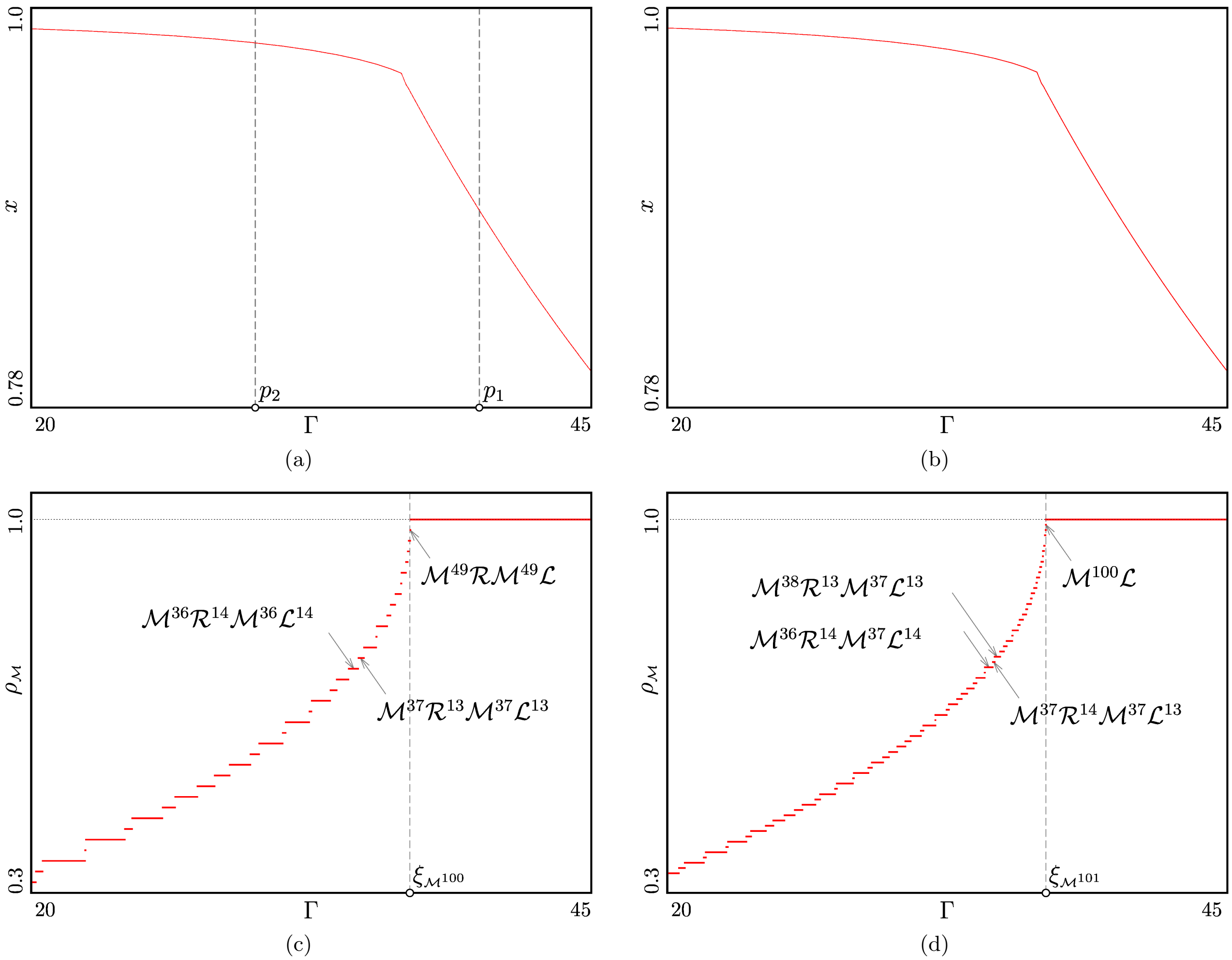

Fig. 9. Transition from the domain $\Pi_1^{(1)}$ to $\Pi_1^{(4)}$ (for decreasing values of Γ) leading to a cascade of persistence border collisions of fixed points of map (11) for (a) $m = 100$; (b) $m = 101$. The corresponding parameter paths are marked in Figs. 10 and 11 with A^1 and A^2, respectively. In (c) and (d) the corresponding ratios $\rho_{\mathcal{M}}$ are shown, some of the associated symbolic sequences are marked. Cycles of map (10) at the parameter points marked with p_1 and p_2 in (a) are shown in Figs. 7(a) and 7(b), respectively.

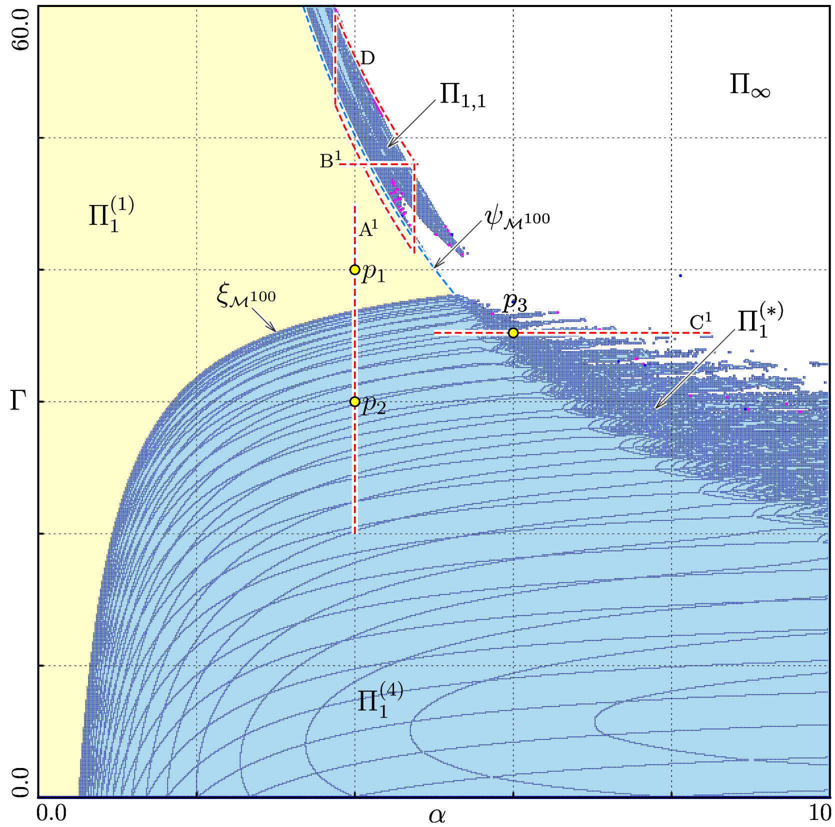

Fig. 10. Sub-domains $\Pi_1^{(1)}$, $\Pi_1^{(4)}$, and $\Pi_1^{(*)}$ of the stability domain Π_1 in the case of the even frequency modulation ratio $m = 100$. The boundaries of the region $\Pi_1^{(1)}$ corresponding to the optimal operational regime of the inverter are given by the persistence border collision curve $\xi_{\mathcal{M}^{100}}$ and the degenerate pitchfork bifurcation curve $\psi_{\mathcal{M}^{100}}$. Inside the $\Pi_1^{(4)}$ the grid-like structure formed by persistence border collision curves is shown. Bifurcation diagrams along the parameter paths marked with A^1, B^1, and C^1 are shown in Figs. 9(a), 13(a), and 12(b), respectively. Cycles of map (10) at the parameter values marked with p_1, p_2, p_3 are shown in Fig. 7(a), (b), (c), respectively.

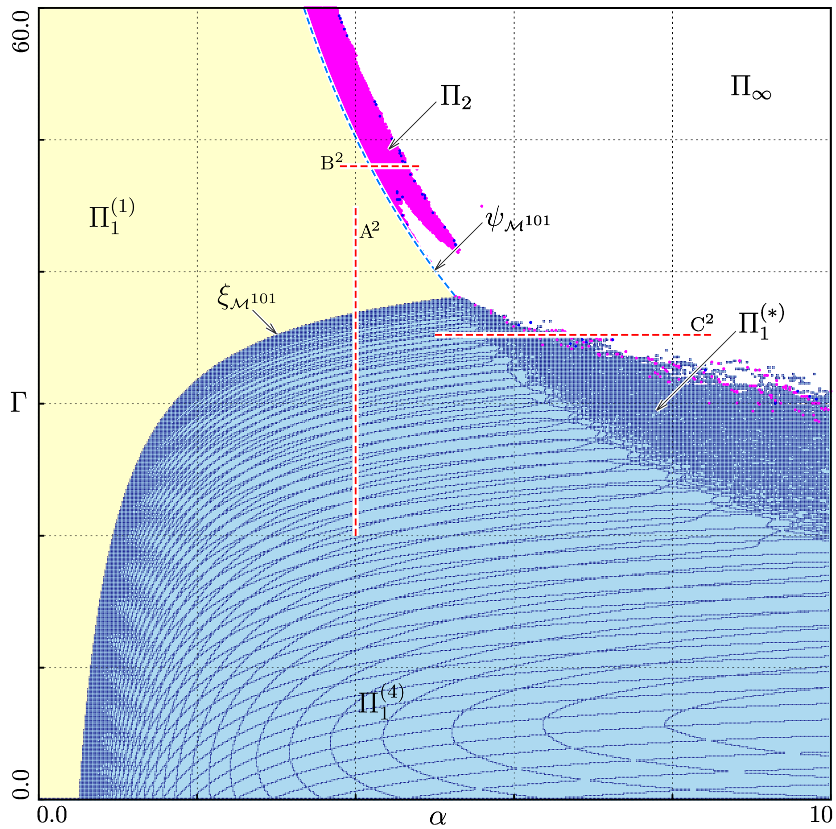

Fig. 11. Sub-domains $\Pi_1^{(1)}$, $\Pi_1^{(4)}$, and $\Pi_1^{(*)}$ of the stability domain Π_1 in the case of the even frequency modulation ratio $m = 101$. The boundaries of the region $\Pi_1^{(1)}$ corresponding to the optimal operational regime of the inverter are given by the persistence border collision curve $\xi_{\mathcal{M}^{101}}$ and the degenerate flip bifurcation curve $\psi_{\mathcal{M}^{100}}$. Inside the $\Pi_1^{(4)}$ the grid-like structure formed by persistence border collision curves is shown. Bifurcation diagrams along the parameter paths marked with A^1, B^1, and C^1 are shown in Figs. 9(b), 13(b), and 12(b), respectively.

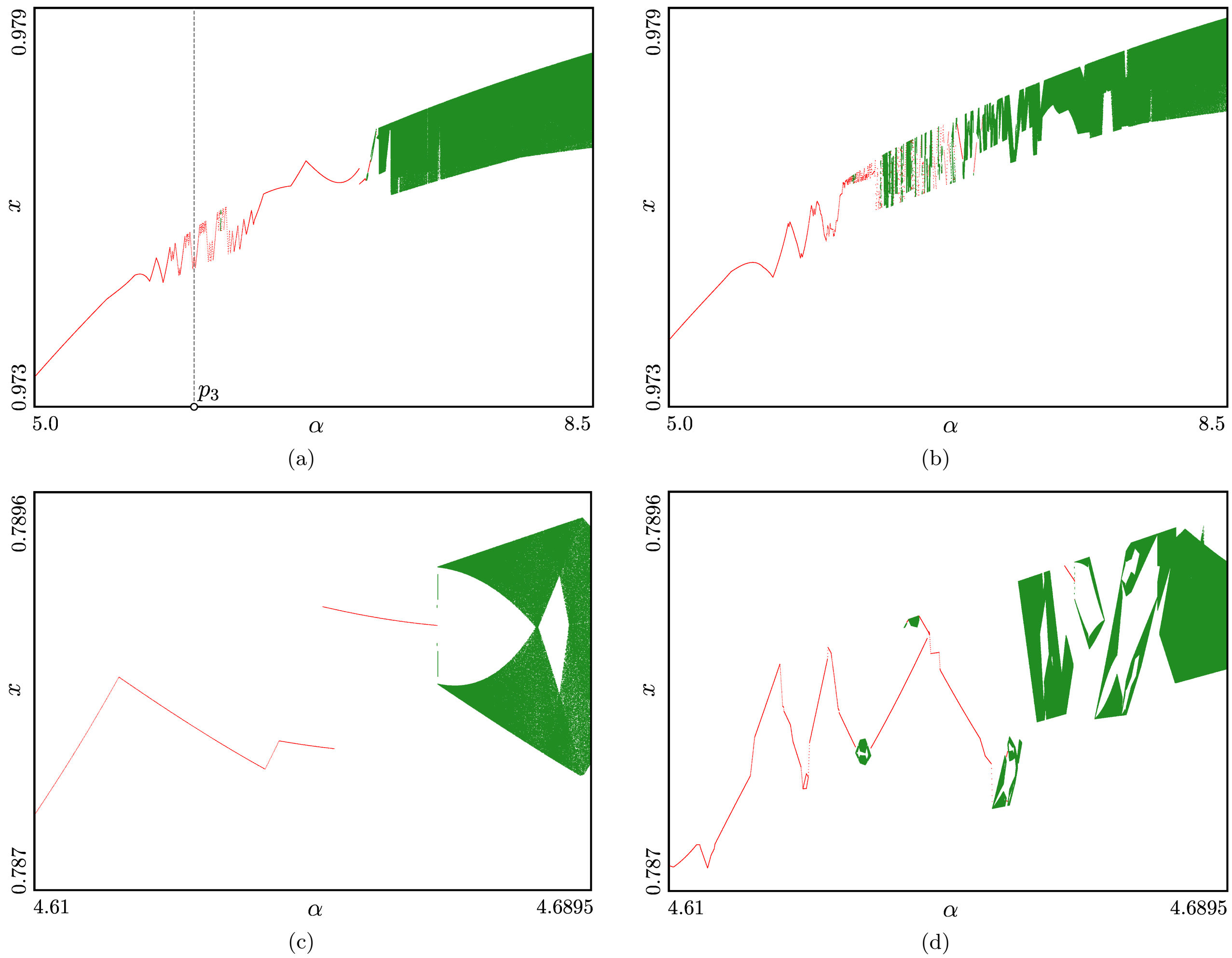

Fig. 12. Transitions to chaos via irregular cascades of border collisions. (a) from the domain $\Pi_1^{(*)}$, $m = 100$; (b) from the domain $\Pi_1^{(*)}$, $m = 101$; The corresponding parameter paths are marked in Figs. 10 and 11 with C^1 and C^2, respectively. (c) from the domain $\Pi_{1,1}$, $m = 100$; (d) from the domain Π_2, $m = 101$; The corresponding regions are outlined by rectangles in Figs. 13(a), (b), respectively. The cycle of map (10) at the parameter point marked with p_3 in (a) is shown in Fig. 7(c).

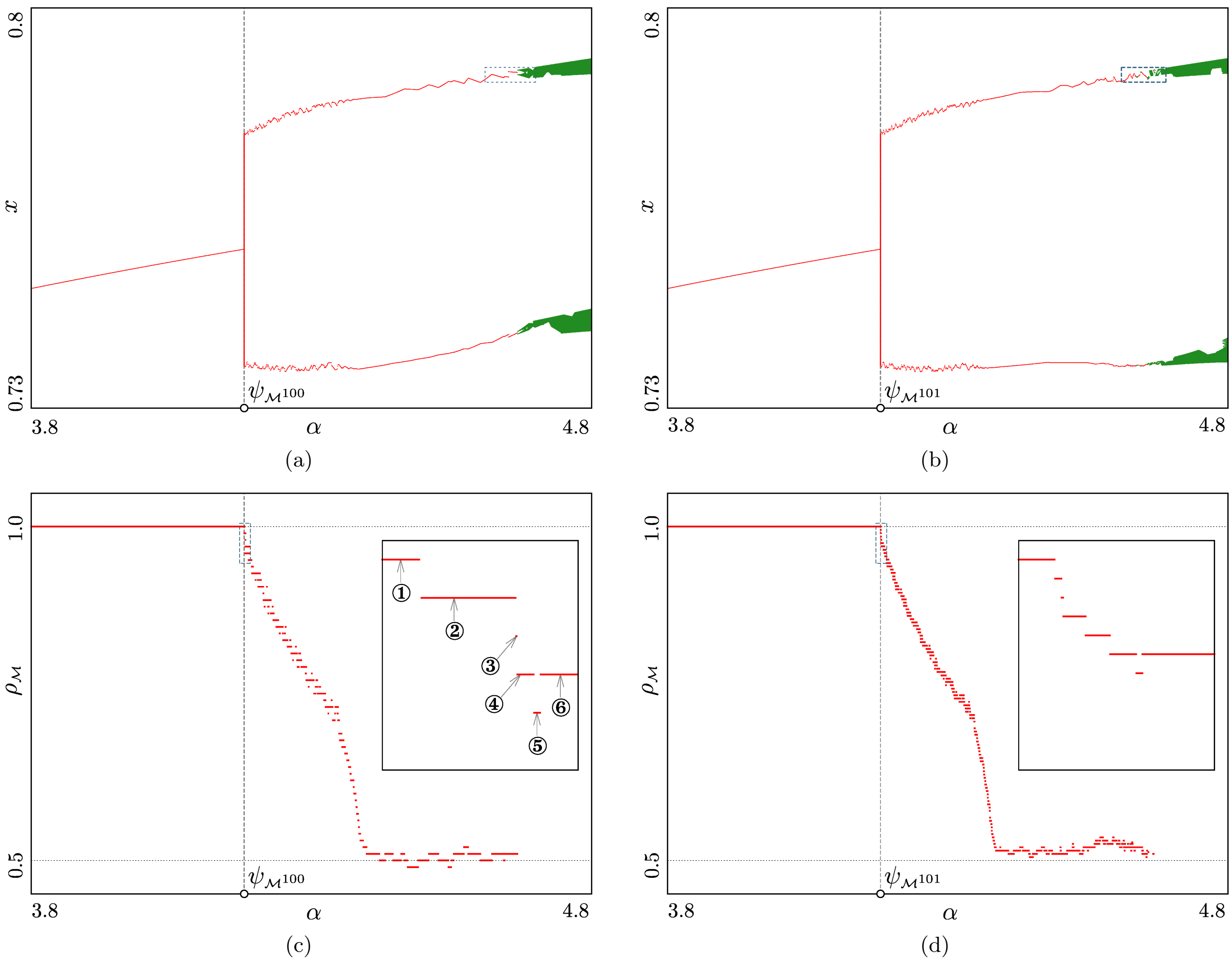

Fig. 13. (a), (c) Transition from the domain $\Pi_1^{(1)}$ to the domain $\Pi_{1,1}^{(1)}$ via a degenerate pitchfork bifurcation at $\psi_{\mathcal{M}^{100}}$, $m = 100$. (b), (d) Transition from the domain $\Pi_1^{(1)}$ to the domain $\Pi_2^{(1)}$ via a degenerate flip bifurcation at $\psi_{\mathcal{M}^{101}}$, $m = 101$. The corresponding parameter paths are marked in Fig. 10 by B^1 and B^2, respectively. In (c) and (d) the ratio $\rho_{\mathcal{M}}$ in the symbolic sequences associated with fixed points (c) and 2-cycles (d) of map f^m are shown. The inset in (c) shows the marked rectangle close to $\psi_{\mathcal{M}^{100}}$ magnified. The symbolic sequences corresponding to the labels ① – ⑥ are given in Eq. 28. $\Gamma = 48.0$.

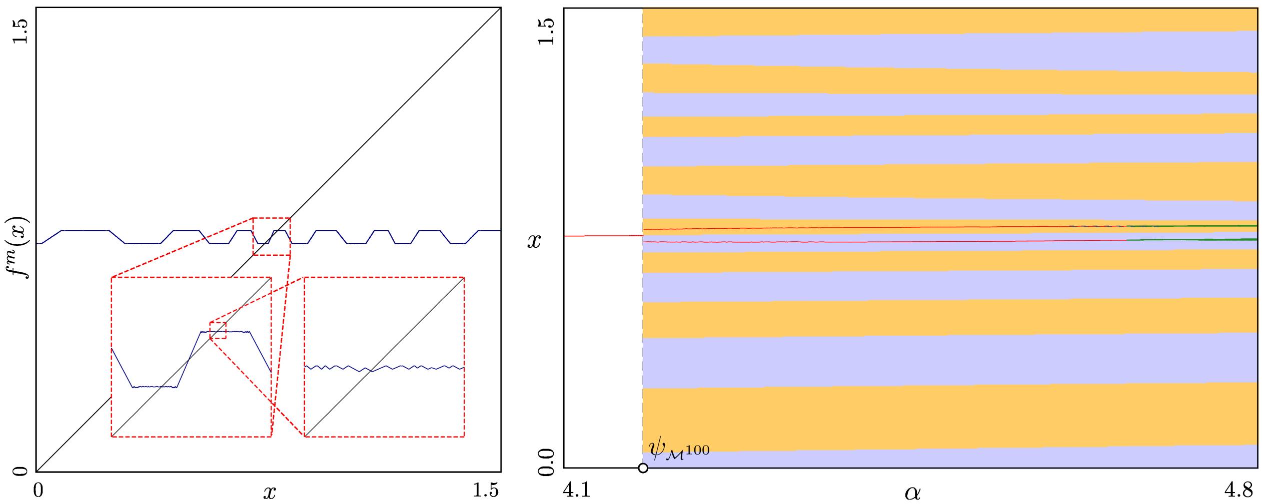

(a) (b)

Fig. 14. (a)The function f^m at $\alpha = 4.2$ (after the degenerate pitchfork bifurcation $\psi_{\mathcal{M}^{100}}$). (b) Basins of attraction of attractors (fixed points as well as chaotic attractors) belonging to the upper and the lower branches in the bifurcation diagram. $m = 100$, $\Gamma = 48.0$.

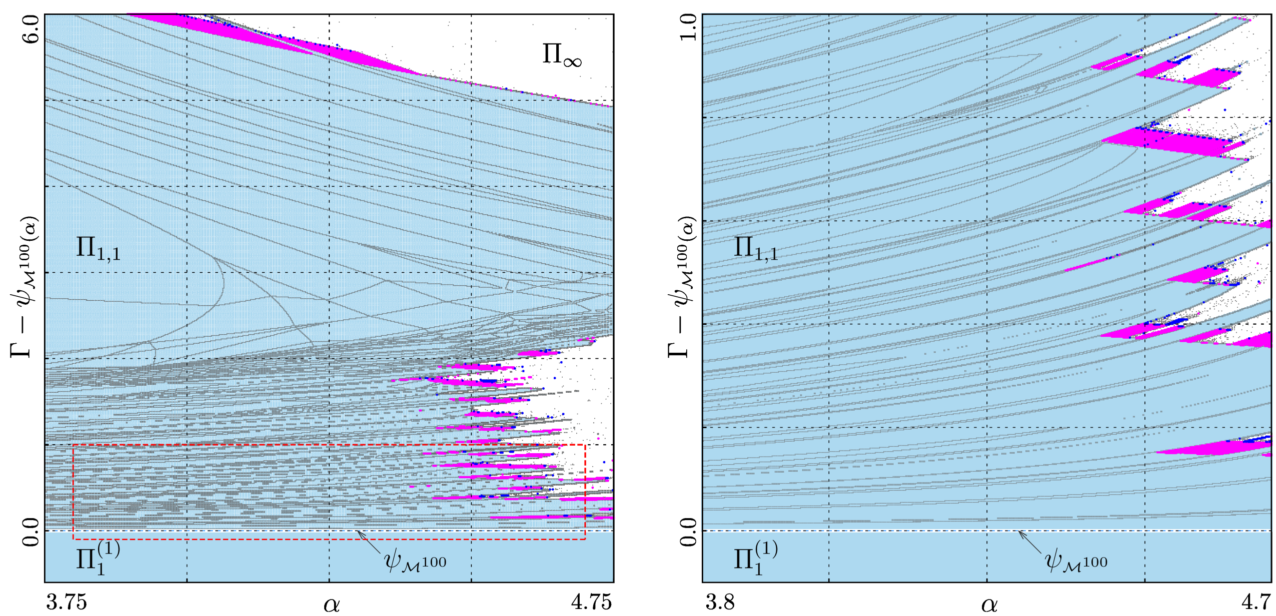

(a) (b)

Fig. 15. Structures formed by persistence border collisions of pairs of cycles inside the bistability region $\Pi_{1,1}$. The presented parameter region is marked in Fig. 10. The vertical axis corresponds to the distance of the actual parameter point from the degenerate pitchfork bifurcation curve $\psi_{\mathcal{M}^{100}}$. The rectangle marked in (a) is shown magnified in (b). $m = 100$.

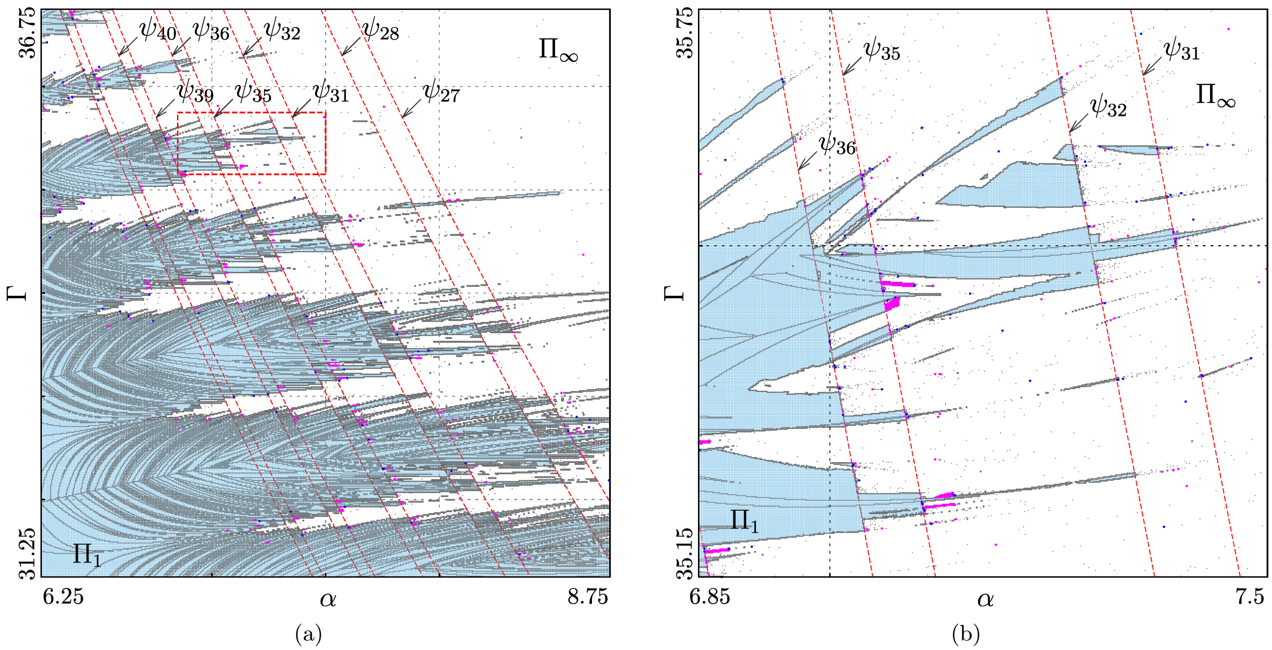

Fig. 16. Alignment of degenerate bifurcation curves. Curves ψ^{27}, ψ^{31}, ψ^{35}, ψ^{39} correspond to degenerate flip, Curves ψ^{28}, ψ^{32}, ψ^{36}, ψ^{40} to degenerate pitchfork bifurcations. The rectangle marked in (a) is shown magnified in (b). $m = 100$.

References

Alexander, A. S. [2016] "Development of solar photovoltaic inverter with reduced harmonic distortions suitable for Indian sub-continent," *Renewable and Sustainable Energy Reviews* **56**, 694–704.

Armstrong-Hélouvry, B., Dupont, P. & Wit, C. D. [1994] "A survey of models, analysis tools and compensation methods for the control of machines with friction," *Automatica* **30**, 1083–1138.

Avrutin, V., Morcillo, J., Zhusubaliyev, Zh. & Angulo, F. [2017a] "Bubbling in a power electronic inverter: Onset, development and detection," *Chaos, Solitons & Fractals* **104**, 135–152.

Avrutin, V., Mosekilde, E., Zhusubaliyev, Zh. & Gardini, L. [2015] "Onset of chaos in a single-phase power electronic inverter," *Chaos* **25**, 043114.

Avrutin, V., Zhusubaliyev, Zh. & Mosekilde, E. [2016] "Border collisions inside the stability domain of a fixed point," *Physica D* **321-322**, 1–15.

Avrutin, V., Zhusubaliyev, Zh. & Mosekilde, E. [2017b] "Cascades of alternating pitchfork and flip bifurcations in H-bridge inverters," *Physica D* **345**, 27–39.

Banerjee, S. & Verghese, G. C. [2001] *Nonlinear Phenomena in Power Electronics – Attractors, Bifurcations, Chaos, and Nonlinear Control* (IEEE Press).

Bischi, G., Chiarella, C., Kopel, M. & Szidarovszky, F. [2010] *Nonlinear oligopolies: Stability and bifurcations* (Springer Science & Business Media).

Brogliato, B. [1999] *Nonsmooth Mechanics*, Communications and Control Engineering (Springer).

di Bernardo, M., Budd, C., Champneys, A. R., Kowalczyk, P., Nordmark, A. B., Piiroinen, P. T. & Olivar, G. [2008a] "Bifurcations in nonsmooth dynamical systems," *SIAM Review* **50**, 629–701.

di Bernardo, M., Budd, C. J., Champneys, A. R. & Kowalczyk, P. [2008b] *Piecewise-smooth Dynamical Systems: Theory and Applications*, Applied Mathematical Sciences, Vol. 163 (Springer).

Espinoza, J. [2011] "Inverters," *Power Electronics Handbook (Third Edition)*, ed. Rashid, M., chap. 10, (Butterworth-Heinemann, Boston), pp. 357 – 408.

Hassaine, L., Olias, E., Quintero, J. & Salas, V. [2014] "Overview of power inverter topologies and control structures for grid connected photovoltaic systems," *Renewable and Sustainable Energy Reviews* **30**, 796–807.

Jain, B., Jain, S. & Nema, R. K. [2015] "Control strategies of grid interfaced wind energy conversion system: an overview," *Renewable and Sustainable Energy Reviews* **47**, 983–996.

Leine, R. & Nijmeijer, H. [2013] *Dynamics and bifurcations of non-smooth mechanical systems*, Vol. 18 (Springer Science & Business Media).

Mosekilde, E. & Laugesen, J. L. [2007] "Nonlinear dynamic phenomena in the beer model," *System Dynamics Review* **23**, 229–252.

Poullikkas, A. [2015] "Sustainable options for electric vehicle technologies," *Renewable and Sustainable Energy Reviews* **41**, 1277–1287.

Puu, T. & Sushko, I. (eds.) [2006] *Business Cycle Dynamics - Models and Tools* (Springer Verlag).

Rashid, M. H. & Luo, F. L. (eds.) [2006] *Power Electronics Handbook* (Elsevier Science).

Sayigh (ed.) [2016] *Renewable Energy in the Service of Mankind*, Vol. II (Springer).

Singh, G. [2013] "Solar power generation by PV (photovoltaic) technology: a review," *Energy* **53**, 1–13.

S.Khomfoi & Tolbert, L. [2011] "Multilevel power converters," *Power Electronics Handbook (Third Edition)*, ed. Rashid, M., "chap. 17," (Butterworth-Heinemann, Boston), pp. 455 – 486.

Sushko, I. & Gardini, L. [2010] "Degenerate Bifurcations and Border Collisions in Piecewise Smooth 1D and 2D Maps," *Int. J. Bifurcation Chaos* **20**, 2045–2070.

Sushko, I., Gardini, L. & Avrutin, V. [2016] "Nonsmooth one-dimensional maps: Some basic concepts and definitions," *J. of Diff. Equations and Applications* **22**, 1816–1870.

Zhusubaliyev, Zh. & Mosekilde, E. [2003] *Bifurcations and Chaos in piecewise-smooth dynamical systems*, Nonlinear Science A, Vol. 44 (World Scientific).